Solar Phys (2009) 256: 3–40
DOI 10.1007/s11207-009-9347-4

Solar Flare and CME Observations with STEREO/EUVI

M.J. Aschwanden · J.P. Wuelser · N.V. Nitta · J.R. Lemen

Received: 4 December 2008 / Accepted: 27 March 2009 / Published online: 21 April 2009

Abstract STEREO/EUVI observed 185 flare events (detected above the GOES class C1 level or at >25 keV with RHESSI) during the first two years of the mission (December 2006 – November 2008), while coronal mass ejections (CMEs) were reported in about a third of these events. We compile a comprehensive catalog of these EUVI-observed events, containing the peak fluxes in soft X rays, hard X rays, and EUV, as well as a classification and statistics of prominent EUV features: 79% show impulsive EUV emission (coincident with hard X rays), 73% show delayed EUV emission from postflare loops and arcades, 24% represent occulted flares, 17% exhibit EUV dimming, 5% show loop oscillations or propagating waves, and at least 3% show erupting filaments. We analyze an example of each EUV feature by stereoscopic modeling of its 3D geometry. We find that EUV emission can be dominated by impulsive emission from a heated, highly sheared, noneruptive filament, in addition to the more common impulsive EUV emission from flare ribbons or the delayed postflare EUV emission that results from cooling of the soft-X-ray-emitting flare loops. Occulted flares allow us to determine CME-related coronal dimming uncontaminated from flare-related EUV emission. From modeling the time evolution of EUV dimming we can accurately quantify the initial expansion of CMEs and determine their masses. Further, we find evidence that coronal loop oscillations are excited by the rapid initial expansion of CMEs. These examples demonstrate that stereoscopic EUV data provide powerful new methods to model the 3D aspects in the hydrodynamics of flares and kinematics of CMEs.

Keywords Solar flares · Coronal mass ejections · EUV · Stereoscopy

STEREO Science Results at Solar Minimum
Guest Editors: Eric R. Christian, Michael L. Kaiser, Therese A. Kucera, O.C. St. Cyr.

M.J. Aschwanden (✉) · J.P. Wuelser · N.V. Nitta · J.R. Lemen
Solar & Astrophysics Laboratory, Lockheed Martin Advanced Technology Center,
Bldg. 252, Org. ADBS, 3251 Hanover St., Palo Alto, CA 94304, USA
e-mail: aschwanden@lmsal.com

1. Introduction

The Extreme UltraViolet Imager (EUVI) (Wuelser *et al.*, 2004) onboard the *Solar-TErrestrial Relations Observatory* (STEREO) spacecraft (Howard *et al.*, 2008, and other articles in volume 136 of *Space Science Reviews*) is the only instrument of this mission that images the lower solar corona (≤ 1.6 solar radii) and thus yields information on the initiation of CMEs and the associated flares. The STEREO mission was designed to rapidly increase the separation angle of the two spacecraft STEREO-Ahead (STEREO-A) and STEREO-Behind (STEREO-B), a design concept that provides classical small-angle stereoscopy only in the initial phase (say $\alpha_{\rm sep} \approx 5^\circ - 30^\circ$ during April – August 2007) and intermediate-angle stereoscopy for up to two years of the mission (say $\alpha_{\rm sep} \approx 30^\circ - 90^\circ$), which are the time periods of observations covered in this study. Future observations will all deal with extremely large stereoscopic angles, where the flare or CME launch site will be occulted and thus invisible to at least one STEREO spacecraft in most cases. Consequently, stereoscopic triangulation in the lower corona will become much rarer in the near future. The EUVI dataset acquired during the first two years of the mission is therefore a unique asset, which we survey and exemplify in this study.

During the first two years of the STEREO mission, EUVI data were used to study the 3D geometry and physical parameters of active region loops (Aschwanden *et al.*, 2008a, 2008b, 2009a; Noglik, Walsh, and Maclean, 2008), the compatibility with magnetic field models (Feng *et al.*, 2007; DeRosa *et al.*, 2009; Sandman *et al.*, 2009), erupting filaments (Li *et al.*, 2008; Gissot *et al.*, 2008), global (EIT) waves (Veronig, Temmer, and Vrsnak, 2008; Long *et al.*, 2008; Attrill *et al.*, 2007), transverse loop oscillations (Verwichte *et al.*, 2009), microflare jets (Chifor *et al.*, 2008), and polar coronal jets and plumes (Patsourakos *et al.*, 2008; Raouafi *et al.*, 2008). In this study we focus on flare and CME-related observations, such as the impulsive and postflare EUV emission, occulted flares, coronal EUV dimming, initial CME expansion, erupting filaments, excitation of coronal loop oscillations, and global waves, phenomena that have thus far been largely unexplored in stereoscopic EUVI data. In this early study we establish a comprehensive EUVI event catalog that may serve other researchers to find suitable events for more focused studies. We will defer more detailed in-depth investigations and modeling of EUVI data to future studies.

2. Description of the EUVI Instrument and Operation

EUVI is a normal incidence EUV telescope (of Ritchey – Chrétien type) with a 2048×2048 pixel detector, a pixel size of $1.59''$, and a field of view out to 1.7 solar radii. It observes in four spectral channels (Fe IX 171 Å, Fe XII 195 Å, Fe XV 284 Å, and He II 304 Å) that span the $T = 0.05 - 20$ MK temperature range. An important feature for the stabilization of EUVI images is the fine pointing system, which compensates for spacecraft jitter down to subarcsecond level. Further technical details on the optics, filters, response functions, and instrument calibration are given in Wuelser *et al.* (2004) and Section 2 of Howard *et al.* (2008). Filter response functions for both the STEREO-A/EUVI and STEREO-B/EUVI instruments and conversion factors of incoming photons to data numbers per second (DN s^{-1}) are also given in Aschwanden *et al.* (2008a). Typical exposure times are 2 – 4 s for 171 Å, 4 – 16 s for 195 Å, and 16 – 32 s for 284 Å.

EUVI images are compressed onboard the spacecraft with the ICER algorithm, which allows one to trade higher image cadence versus lower image quality. Typical compression factors used are in the order of 20 – 40, without degrading the image quality more than the

photon noise in areas that record more than a few photons per pixel. The EUVI is typically operated in one of two modes: synoptic or campaign. The basic EUVI synoptic mode has a fast cadence of 2.5 min for 171 Å, a slower cadence of 10 min for 195 and 304 Å, and 20 min for 284 Å. A higher cadence of 75 s for 171 Å and 5 min in the other wavelengths was used during special campaigns (for two weeks in May 2007). Also, a ring buffer records EUVI images with a higher cadence during up to 4 hours per day; these are downloaded when extra telemetry is available.

Data analysis of EUVI images can be performed with Interactive Data Language (IDL) software that was put online in the Solar Software (SSW) package, described in a tutorial that can be found on the Web site http://secchi.lmsal.com/EUVI/. This package includes software to obtain EUVI images, to coalign stereoscopic EUVI image pairs, and to perform 3D reconstruction of curvilinear features (such as loops and filaments). What is different for the STEREO spacecraft compared with TRACE or SOHO/EIT, which all have the same EUV wavelength channels, is the distance, aspect angle, and orientation of the spacecraft with respect to Sun center (typically in the range of $\approx 0.9 - 1.1$ AU), which need to be considered in image coalignments. Some software allows one to coalign a stereoscopic image pair (from A and B) into the reference system of the same spacecraft, where the horizontal image axis is aligned with the epipolar plane (defined by the two spacecraft positions and Sun center), which is most useful in carrying out stereoscopic triangulation. The epipolar plane is generally not identical with the ecliptic plane, because the two STEREO spacecraft have orbits oscillating above and below the ecliptic plane, but coordinate transformations of images into heliospheric coordinates can be carried out by using the information in the FITS headers of the EUVI images (see also documents on data processing and analysis on the SECCHI Wiki Web page http://secchi.nrl.navy.mil/wiki/).

3. Monthly Statistics of Flares and CMEs

Although the first two years (2007 – 2008) of the STEREO mission coincide with the minimum of the solar cycle, over hundred flares and CME events have been observed with the full-disk EUVI telescope. Table 1 shows a monthly compilation of flare events reported by GOES and the Ramaty High-Energy Solar Spectroscopic Imager (RHESSI; Lin *et al.*, 2002; for RHESSI flare list see http://hesperia.gsfc.nasa.gov/rhessidatacenter/) as well as CME events reported by LASCO (http://cdaw.gsfc.nasa.gov/CME_list/) onboard SOHO and by Cor-1 (http://cor1.gsfc.nasa.gov/catalog) or Cor-2 onboard STEREO/SECCHI, from the beginning of the STEREO mission (*i.e.*, opening of EUVI doors on 4 December 2006 for the Ahead and 12 December 2006 for the Behind spacecraft) to the time of this writing (4 November 2008). A total of 90 flares have been detected with GOES above the C-class level, but only 11 M-class flares and no X-class flares were detected. RHESSI detected some 171 flare events with energies > 25 keV. The flare activity during the two years 2007 – 2008 is very intermittent, essentially clustered within a few active months (December 2006 and January, May, June, and December 2007). Almost no C-class flares occurred during 2008, which seems to be the quietest year in the minimum of the solar cycle, and only a few B- and A-class events were reported by GOES. The reported CME rate is somewhat more steady, averaging ≈ 15 events per month in the LASCO catalog (excluding events labeled as "poor" and "very poor events") and ≈ 36 events per month automatically detected with the Solar Eruptive Event Detection System (SEEDS; http://spaceweather.gmu.edu/seeds/). Similarly, the Computer Aided CME Tracking (CACTUS) catalog (http://sidc.oma.be/cactus/) reported an average of ≈ 22 CME events per month from SECCHI-A/Cor-2 and ≈ 17 CME events per month from SECCHI-B/Cor-2.

Table 1 Monthly statistics of detected flares (with GOES and RHESSI) and CMEs (by LASCO and STEREO/Cor-2) during the first two years of the STEREO mission.

Month	GOES M	GOES C	RHESSI > 25 keV	LASCO CMEs	LASCO SEEDS	Cor-2/A CACTUS	Cor-2/B CACTUS
2006 Dec	0	5	4	31	86	...	...
2007 Jan	0	11	12	30	50	...	...
2007 Feb	0	3	1	23	59	...	...
2007 Mar	0	0	1	23	...	21	22
2007 Apr	0	1	7	15	25	14	5
2007 May	0	6	19	27	61	34	29
2007 Jun	10	16	57	25	38	24	17
2007 Jul	0	19	4	17	49	27	21
2007 Aug	0	3	2	16	24	30	12
2007 Sep	0	0	0	6	28	18	14
2007 Oct	0	0	1	5	19	14	19
2007 Nov	0	0	0	3	17	11	11
2007 Dec	0	11	54	9		22	14
2008 Jan	0	3	2	11	34	13	28
2008 Feb	0	0	0	6	37	26	15
2008 Mar	1	0	5	8	35	17	22
2008 Apr	0	1	1	13	18	26	20
2008 May	0	0	0	5	19	31	16
2008 Jun	0	0	0	10	22	15	12
2008 Jul	0	0	0	...	...	19	11
2008 Aug	0	0	0	...	...	...	...
2008 Sep	0	0	0	...	...	...	...
2008 Oct	0	0	0	...	...	...	...
2008 Nov	0	1	1	...	...	...	...
events	11	80	171	283	621	372	288
per month	0.5	3.3	7.3	14.9	36.5	21.9	16.9

We inspected the SECCHI/EUVI images during all times of GOES C-class or RHESSI > 25 keV flare occurrences, which amounts to 185 events (see the catalog at http://secchi.lmsal.com/EUVI/euvi_events.txt), and found in virtually all cases flare-related EUV emission and postflare loops, but a few events even exhibit significant EUV dimming, EIT waves, and loop oscillations. Overview plots of the flare GOES and EUVI light curves as well as EUVI running-difference images of all 185 events can be found at http://secchi.lmsal.com/EUVI/EVENTS/. The corresponding EUVI movies in all four wavelengths (171, 195, 284, and 304 Å) are also provided in form of anaglyph movies (for small spacecraft separation angles during 2007) or two-panel displays (for large separation angles during 2008); see http://secchi.lmsal.com/EUVI/).

4. EUVI Catalog of Flare and CME Events

The first two years of the STEREO mission are a unique period, because this is the only phase of the mission when the spacecraft separation angle is small to moderate (*i.e.*,

$\alpha_{sep} \lesssim 45°$ at the end of 2007 and $\alpha_{sep} \lesssim 90°$ at the end of 2008, respectively). Because of this unique constellation when classical stereoscopy is feasible, we provide for the benefit of future detailed analysis a complete catalog of 185 flare/CME events observed with EUVI during this mission phase (Table 2). This catalog list contains the following properties of each event: a chronological identification number (1, ..., 185), the date and approximate time interval (bracketing the impulsive and postflare phase), the approximate heliographic location (in longitude and latitude with respect to Sun center), the spacecraft separation angle at the time of the event, the GOES flare classification, the highest detected energy range E with RHESSI (using the 3 – 6, 6 – 12, 12 – 25, 25 – 50, 50 – 100 keV energy bands from the RHESSI flare catalog), the RHESSI peak count rate P (in counts/s in the energy range of 12 – 25 keV, averaged over active collimators, including background), the peak STEREO-A/EUVI and STEREO-B/EUVI count rate (in DN s^{-1} integrated over a flare-encompassing area of 256 × 256 pixels, with subtraction of the flare-unrelated background flux, defined by the minimum of the EUVI time profile), a classification of EUVI features (based on visual inspection), and CME events reported by SOHO/LASCO or Cor-1 and Cor-2 of STEREO/SECCHI. The classification of EUVI features contains EUV emission from the impulsive flare phase (I), EUV emission from postflare loops (P), EUV dimming (D), occultation for one or both STEREO-A and STEREO-B spacecraft (O), waves or loop oscillations (W), eruptive features (E), and a flag for test images or poor image quality (T). Impulsive EUV emission is identified from an EUV flux increase that coincides with the peak of hard X rays (or the time derivative of the soft X-ray emission according to the Neupert effect) and is generally manifested in brightenings of compact flare kernels in the EUV images. Postflare emission generally originates from entire loops or loop arcades, but it always appears with a delay with respect to the impulsive phase, because the flare plasma has to first cool from soft X-ray to EUV temperatures. The detection of dimming and waves or loop oscillations is very threshold dependent and thus our primary inspection as listed in Table 2 may represent a lower limit only; additional events with such features may be found in future more detailed data analysis.

A breakdown of the features detected so far in EUVI events is given in Table 3: Impulsive EUVI emission is detected in ≈79%, postflare loop emission in ≈73%, partially occulted events in ≈24%, EUV dimming in ≈17%, waves and loop oscillations in ≈5%, and eruptive features in ≈3%. In the following sections we present a few examples of flare and CME events with the identified features; a more comprehensive analysis will be the subject of future studies.

5. EUV Emission from the Impulsive Flare Phase

Impulsive EUV emission seems to be quite common in flares, since we found a simultaneous increase of EUV and soft X rays in the impulsive flare phase in ≈79% of the analyzed events. However, the delayed EUV emission of postflare loops is often more dominant in peak flux and fluence (*i.e.*, time-integrated flux).

The flare event of 10 June 2007, at 11:10 UT (event 106 in Table 2), a modest GOES C1.9-class flare, represents one of the cleanest examples of dominant EUV emission during the impulsive flare phase. The peak of the EUV emission coincides closely with the peak of the soft X rays or hard X rays (Figure 1 top), for which we computed a proxy from the time derivative of the soft X rays (according to the Neupert effect). Hence we conclude that the dominant EUV emission is intimately related to the maximum heating rate (which supposedly coincides with the hard X-ray peak), rather than to the cooling of postflare loops (which normally occurs significantly later). But how can that be?

Table 2 Flare and CME catalog of STEREO/EUVI observations.

No.	Date	Time (UT)	Heliogr. location	Stereo angle (deg)	GOES class	RHESSI[a] E (keV)	RHESSI[a] P (counts s^{-1})	EUVI[b] A (10^5 DN^{-1})	EUVI[b] B	EUVI[b] Com.	CME[c] Rep.
1	06/12/04	17:00 – 17:30	S06E76	0.0	C1.2	25	300	?	...	T	...
2	06/12/06	14:55 – 15:40	S06E60	0.0	C1.7	...	...	3.3	...	P	...
3	06/12/06	15:30 – 16:40	S06E60	0.0	C1.4	...	...	7.9	...	P	...
4	06/12/09	10:20 – 12:00	S05E19	0.0	C1.3	12	52	8.3	...	I	...
5	06/12/31	07:00 – 12:00	S00E80	0.0	C1.3	12	101	18.6	14.9	P	...
6	07/01/10	09:10 – 12:00	S02W62	0.2	C1.7	3	16	...	14.9	IP	...
7	07/01/11	00:50 – 02:30	S01W75	0.2	C1.0	12	77	15.3	...	IP	...
8	07/01/12	01:00 – 03:00	N00W87	0.2	C1.5	12	34	31.2	...	IPEW	L
9	07/01/15	02:00 – 05:00	N05E47	0.3	C1.4	12	17	17.8	15.9	P	L
10	07/01/16	02:00 – 04:00	N04E33	0.3	C4.2	...	...	17.7	?	P	L
11	07/01/16	16:00 – 17:00	N06E27	0.3	C1.1	12	92	6.0	?	P	L
12	07/01/21	05:00 – 06:00	S03W22	0.4	B9	12	68	10.0	8.1	I	L
13	07/01/21	13:00 – 14:00	S03W25	0.4	C2.3	12	80	14.1	11.1	I	...
14	07/01/24	13:30 – 20:00	S22E89	0.5	B9.0	3	30	8.1	5.7	PDO	LS
15	07/01/24	18:50 – 19:50	S02W69	0.5	B3.1	12	15	7.3	6.1	P	...
16	07/01/25	05:00 – 06:00	S02W73	0.5	B3.5	12	76	...	5.5	I	...
17	07/01/25	06:00 – 10:00	S08E87	0.5	C6.3	12	20	...	23.3	PO	LS
18	07/01/29	16:30 – 18:30	N00E38	0.6	C3.4	12	26	8.3	7.5	IP	L
19	07/01/29	22:20 – 23:59	N01E35	0.6	C1.5	12	56	4.0	3.3	PD	...
20	07/01/30	07:20 – 08:20	S06E28	0.6	C1.0	12	38	14.1	8.4	IP	...
21	07/02/08	22:30 – 23:59	S24W90	0.7	C1.2	...	...	3.8	3.6	PO	L
22	07/02/16	01:30 – 04:30	S24E90	0.8	C1.7	...	...	13.9	11.9	IPO	LS
23	07/02/18	19:20 – 21:00	S07E20	0.9	B8.3	...	...	13.4	13.8	I	L
24	07/02/19	00:00 – 01:00	S10E16	0.9	C1.1	3	16	4.9	4.4	I	S

Table 2 (*Continued.*)

No.	Date	Time (UT)	Heliogr. location	Stereo angle (deg)	GOES class	RHESSI[a] E (keV)	RHESSI[a] P (counts s^{-1})	EUVI[b] A (10^5 DN^{-1})	EUVI[b] B	EUVI[b] Com.	CME[c] Rep.
25	07/02/24	12:00 – 16:00	N11E80	1.1	A5	3	28	5.8	4.9	PDO	LS
26	07/02/27	07:10 – 08:10	S00E21	1.2	B3	12	16	6.1	5.5	I	...
27	07/03/31	01:10 – 01:50	N10E35	3.0	B2.2	...	...	2.5	...	PE	...
28	07/04/24	22:40 – 23:59	S27E87	5.4	C2.8	12	68	14.5	...	PO	...
29	07/04/25	05:30 – 06:00	S27E89	5.4	B4	12	20	3.5	3.7	IEDO	LS
30	07/04/26	02:15 – 03:00	S27E88	5.5	B1	12	11	24.8	3.8	PD	S
31	07/04/27	05:10 – 06:00	S22E61	5.6	B6.2	12	36	4.4	3.4	P	L
32	07/04/28	04:05 – 04:50	S20E47	5.7	B2.3	12	24	3.7	2.9	IP	L
33	07/04/28	23:10 – 23:59	S18E37	5.8	B2	12	27	3.8	3.0	P	L
34	07/05/01	03:30 – 04:30	S14E08	6.1	B1.7	12	16	4.7	5.4	IP	L
35	07/05/02	23:20 – 23:59	S09W16	6.3	C8.5	12	30	23.0	17.3	IPW	...
36	07/05/04	18:00 – 19:00	S10W39	6.6	B3	12	35	6.0	119.8	IP	L
37	07/05/05	12:15 – 13:40	S11W51	6.7	C4.2	12	18	44.3	19.5	IP	S
38	07/05/08	13:15 – 14:00	S13W87	7.1	B2	12	14	27.4	5.9	IDO	...
39	07/05/08	23:00 – 23:59	S13W87	7.1	B2.4	12	13	8.0	4.1	IPDO	LS
40	07/05/15	15:20 – 16:00	N00E50	8.1	C1	...	...	5.9	3.9	PD	L
41	07/05/15	17:55 – 18:50	N02E51	8.1	B3.2	12	80	16.8	15.0	IPD	LS
42	07/05/16	01:40 – 02:30	N02E47	8.1	B2	12	15	2.5	1.5	IP	L
43	07/05/16	17:10 – 18:10	N03E34	8.2	C2.9	12	26	12.7	9.9	IPDW	LS
44	07/05/17	12:40 – 13:40	N03E24	8.3	B5.5	12	35	10.9	8.0	IP	...
45	07/05/18	07:35 – 08:05	N02E16	8.5		12	16	1.1	1.4	I	...
46	07/05/19	12:40 – 13:20	N03W03	8.6	B1.3	12	46	17.4	13.9	IPEDW	LS
47	07/05/23	01:30 – 02:30	N02W48	9.2	B2.8	12	26	8.5	5.7	IP	...
48	07/05/23	07:10 – 08:20	N00W53	9.2	B5.3	12	22	161.6	7.5	PD	S
49	07/05/26	17:20 – 18:20	S05W90	9.7		12	56	8.2	4.6	PDO	L

Table 2 (*Continued.*)

No.	Date	Time (UT)	Heliogr. location	Stereo angle (deg)	GOES class	RHESSI[a] E (keV)	RHESSI[a] P (counts s^{-1})	EUVI[b] A (10^5 DN^{-1})	EUVI[b] B	EUVI[b] Com.	CME[c] Rep.
50	07/05/30	13:40 – 14:40	S27E87	10.4	C2	12	42	?	?	IT	...
51	07/05/31	12:30 – 13:30	S27E87	10.5	C1.1	12	20	5.1	6.5	IPDO	L
52	07/05/31	17:57 – 18:50	S27E87	10.6	B3.7	12	18	2.7	6.9	PDO	L
53	07/05/31	22:10 – 23:10	S27E87	10.6	B5.4	12	18	3.0	3.5	PDO	...
54	07/06/01	06:40 – 07:40	S17E90	10.6	M1	...	...	8.1	16.0	PDO	L
55	07/06/01	14:30 – 15:30	S07E87	10.7	M2.8	12	64	20.6	18.8	PO	...
56	07/06/01	16:50 – 17:50	S08E85	10.7	B3.3	12	13	5.1	4.7	PO	...
57	07/06/01	17:40 – 18:20	S07E85	10.7		12	14	5.7	4.4	PO	...
58	07/06/01	20:05 – 20:35	S07E83	10.7	B2.2	12	12	1.9	2.0	IPO	...
59	07/06/01	21:35 – 22:35	S07E82	10.7	M2.1	50	2544	17.0	16.6	IPO	LS
60	07/06/02	05:20 – 06:50	S08E87	10.8	M2.5	25	1866	49.4	41.9	P	L
61	07/06/02	07:50 – 08:50	S06E74	10.8	B3.6	12	80	3.2	4.0	IP	...
62	07/06/02	09:10 – 10:20	S07E73	10.8	B1.9	12	60	2.4	1.7	IP	...
63	07/06/02	10:20 – 11:20	S05E74	10.8	M1	25	624	13.8	12.9	IP	...
64	07/06/02	17:10 – 17:40	S07E71	10.9		12	14	...	1.9	I	L
65	07/06/03	00:20 – 01:20	S05E66	10.9	B4.7	12	13	4.1	3.4	IP	...
66	07/06/03	01:20 – 01:50	S08E68	10.9	B8.8	12	112	2.6	2.6	I	...
67	07/06/03	01:40 – 02:06	S07E68	10.9	M2.4	12	15	28.0	30.7	I	...
68	07/06/03	02:06 – 02:30	S07E68	10.9	M7	12	72	38.4	51.5	IP	...
69	07/06/03	02:25 – 03:30	S15E69	10.9	C1.6	3	18	54.5	46.7	P	...
70	07/06/03	04:00 – 05:00	S05E67	11.0	B9.5	12	30	5.0	4.9	P	L
71	07/06/03	06:30 – 08:10	S04E63	11.0	M4.5	12	20	38.2	31.0	IP	LS
72	07/06/03	09:00 – 10:00	S08E67	11.0	C5.3	50	378	23.0	22.4	IP	LS
73	07/06/03	11:00 – 12:00	S04E60	11.0	B3.3	12	18	3.2	3.0	IP	...
74	07/06/03	18:05 – 19:00	S06E59	11.1	B1.6	12	46	6.9	3.3	IP	...

Table 2 (*Continued.*)

No.	Date	Time (UT)	Heliogr. location	Stereo angle (deg)	GOES class	RHESSI[a]		EUVI[b]			CME[c]
						E (keV)	P (counts s^{-1})	A (10^5 DN^{-1})	B	Com.	Rep.
75	07/06/03	20:10 – 21:00	S08E54	11.1	B5.5	12	34	5.5	7.2	IP	…
76	07/06/04	02:10 – 03:40	S07E58	11.1	B1.5	12	13	15.8	10.4	IP	…
77	07/06/04	04:30 – 05:00	S05E51	11.1	B5	12	38	8.0	6.8	IP	…
78	07/06/04	05:00 – 06:30	S05E50	11.1	M8.9	12	52	97.0	80.2	IP	L
79	07/06/04	07:00 – 07:30	S06E51	11.2	B5.6	12	26	5.8	4.7	IP	…
80	07/06/04	11:50 – 12:20	S06E48	11.2	B2.7	12	12	6.9	5.5	IP	…
81	07/06/04	15:50 – 16:20	S08E45	11.2	B2.7	12	28	2.7	1.9	IP	L
82	07/06/04	18:40 – 19:00	S07E42	11.2	B2.5	12	32	2.4	2.1	IP	…
83	07/06/04	21:00 – 22:00	S08E42	11.2	B3.7	12	14	1.6	1.4	D	…
84	07/06/05	04:10 – 04:50	S08E37	11.3	C1.2	12	30	5.7	4.7	IP	…
85	07/06/05	04:50 – 05:20	S04E27	11.3	B1.6	12	4	2.7	1.9	I	…
86	07/06/05	15:40 – 17:00	S08E31	11.4	C6.6	12	76	21.5	16.4	P	L
87	07/06/06	04:20 – 05:20	S08E22	11.5	B2.8	12	32	7.4	6.8	P	L
88	07/06/06	13:10 – 14:40	S08E17	11.5	B3.1	12	14	3.9	3.2	IP	L
89	07/06/06	17:10 – 18:10	S07E16	11.6	C9.7	3	1	35.7	28.0	IP	…
90	07/06/06	23:00 – 23:59	S08E12	11.6	C1.7	12	68	8.9	…	IP	…
91	07/06/07	00:10 – 01:00	S08E12	11.6	B7.6	12	36	4.2	3.0	I	…
92	07/06/07	01:00 – 02:00	S08E06	11.6	B6.6	12	30	8.5	6.3	IP	…
93	07/06/07	06:20 – 07:20	S09E08	11.7	C1.7	12	104	18.7	15.1	IP	…
94	07/06/07	10:00 – 11:00	S07E06	11.7	C1.1	12	112	10.6	8.7	IP	L
95	07/06/07	17:00 – 18:00	S07E02	11.7	B9.7	3	11	6.4	6.4	IP	L
96	07/06/08	01:20 – 02:20	S08W01	11.8	C1.6	12	44	21.0	15.8	IP	…
97	07/06/08	04:00 – 05:00	S09W03	11.8	C2.3	12	109	9.6	7.4	IP	…
98	07/06/08	04:50 – 05:20	S08W04	11.8	C1.4	12	64	9.4	7.0	IP	LS
99	07/06/08	08:10 – 10:00	S09W10	11.8	C2.9	12	60	38.2	27.0	IPD	L
100	07/06/08	12:30 – 13:30	S08W08	11.9	B7.6	12	28	7.9	5.9	IPDW	LS

Table 2 (*Continued.*)

No.	Date	Time (UT)	Heliogr. location	Stereo angle (deg)	GOES class	RHESSI[a] E (keV)	RHESSI[a] P (counts s^{-1})	EUVI[b] A (10^5 DN^{-1})	EUVI[b] B	EUVI[b] Com.	CME[c] Rep.
100	07/06/08	12:30 – 13:30	S08W08	11.9	B7.6	12	28	7.9	5.9	IPDW	LS
101	07/06/08	14:00 – 15:00	S06W12	11.9	C1.5	3	40	12.2	9.9	PD	...
102	07/06/08	23:00 – 23:59	S10W14	12.0	B2.2	12	28	20.4	14.5	ID	...
103	07/06/09	09:00 – 10:00	S09W25	12.0	B8.6	12	30	15.3	10.4	I	...
104	07/06/09	13:20 – 14:40	S10W23	12.1	M1	12	184	69.4	45.8	IW	L
105	07/06/09	23:00 – 23:59	S11W34	12.1	B6.6	12	12	3.7	6.5	I	L
106	07/06/10	11:00 – 12:00	S10W39	12.2	C1.9	12	28	31.7	21.3	I	...
107	07/06/10	18:30 – 19:30	S09W43	12.3	B1.1	12	16	2.6	2.7	I	...
108	07/06/10	23:00 – 23:59	S11W48	12.3	B8.1	12	20	2.4	1.0	I	...
109	07/06/27	17:30 – 18:30	S20E89	15.4	C1.3	3	34	2.9	2.4	IDOW	...
110	07/06/29	20:00 – 20:30	S06E57	15.8	C1.1	3	32	6.5	4.7	IP	...
111	07/07/07	10:50 – 11:50	S06E87	17.3	B9.1	12	12	2.6	1.6	IDO	...
112	07/07/07	13:50 – 15:00	S05E90	17.3	C1.9	3	114	7.7	9.0	IPO	L
113	07/07/08	13:20 – 14:10	S06E90	17.5	C1.1	...	...	6.2	4.3	IP	...
114	07/07/08	15:50 – 16:20	S18E77	17.5	C1	3	52	4.3	5.6	IPO	L
115	07/07/08	16:40 – 17:20	S18E78	17.5	C1.1	...	...	7.8	5.6	IPO	L
116	07/07/09	01:40 – 02:10	S18E69	17.6	C1	3	22	3.6	3.8	PD	...
117	07/07/09	05:30 – 06:30	S07E62	17.6	C1.7	3	18	8.8	7.0	IP	...
118	07/07/09	22:30 – 23:10	S07E56	17.7	C1.3	3	100	9.5	7.4	IP	L
119	07/07/10	00:50 – 01:20	S06E52	17.8	C3.8	...	...	14.2	11.5	IP	...
120	07/07/10	01:30 – 02:00	S09E52	17.8	C4.3	3	4	8.2	6.8	IP	...
121	07/07/10	03:20 – 03:50	S07E53	17.8	C4.4	3	10	7.2	6.7	IPE	...
122	07/07/10	04:40 – 05:10	S09E52	17.8	C1.2	3	48	14.1	11.9	IP	...
123	07/07/10	06:10 – 06:40	S07E51	17.8	C1.4	3	104	7.9	6.7	IP	...
124	07/07/10	07:00 – 07:30	S04E50	17.8	C7.4	...	...	10.5	9.9	IP	...
125	07/07/10	07:30 – 08:10	S04E49	17.8	C2.8	3	26	15.1	12.6	IP	L

Table 2 (*Continued.*)

No.	Date	Time (UT)	Heliogr. location	Stereo angle (deg)	GOES class	RHESSI[a]		EUVI[b]			CME[c]
						E (keV)	P (counts s^{-1})	A (10^5 DN^{-1})	B	Com.	Rep.
126	07/07/10	11:00 – 11:40	S04E47	17.9	C1.9	3	20	1.7	4.2	IP	…
127	07/07/10	12:30 – 13:00	S04E47	17.9	C8.2	3	549	…	6.3	IP	L
128	07/07/10	17:40 – 18:10	S07E45	17.9	C5.2	3	288	11.2	8.8	IP	…
129	07/07/10	20:40 – 21:10	S10E42	17.9	C1.8	3	8	6.3	5.7	IP	…
130	07/07/10	22:30 – 23:00	S06E41	17.9	C1	3	27	4.3	3.9	IP	…
131	07/07/18	13:40 – 14:10	S05W64	19.5	B1.9	12	18	3.6	1.9	I	…
132	07/08/06	09:00 – 09:30	S11E41	23.3	C1.5	12	46	6.3	5.9	IP	L
133	07/08/06	15:20 – 15:50	S12E38	23.3	C1.1	12	32	7.8	25.2	IPW	LS
134	07/08/24	07:40 – 08:10	S06E41	26.9	C2.1	3	10	11.7	8.9	IP	…
135	07/12/02	19:50 – 20:20	S05E55	42.0	B7	12	1200	6.2	6.5	IP	…
136	07/12/09	15:40 – 16:20	S10E31	42.6	B9.4	12	21	4.1	3.4	IP	…
137	07/12/09	16:40 – 17:10	S10E31	42.6	B8.4	12	32	12.0	10.8	IP	…
138	07/12/10	06:50 – 07:20	S10E24	42.6	B7	12	2416	5.2	4.5	IPD	…
139	07/12/10	11:30 – 12:00	S06E20	42.7	B3.5	12	560	6.5	5.2	I	…
140	07/12/10	13:30 – 14:00	S06E18	42.7	B3.5	12	288	2.8	2.6	PD	L
141	07/12/11	13:10 – 13:40	S10E06	42.7	B3.3	12	624	5.7	5.3	I	…
142	07/12/12	02:00 – 02:30	S07W00	42.8		12	200	4.8	2.7	I	…
143	07/12/13	01:10 – 01:40	S06W12	42.9	B4.3	12	1072	5.8	4.4	I	…
144	07/12/13	04:20 – 04:50	S06W14	42.9	B4.6	12	1322	3.0	1.5	IP	…
145	07/12/13	09:30 – 10:10	S07W21	42.9	C4.5	3	104	15.0	9.8	IP	…
146	07/12/13	11:30 – 12:00	S08W19	42.9	B2.2	12	624	6.4	4.2	I	…
147	07/12/13	13:50 – 14:30	S09W21	42.9	C1	6	784	17.1	10.7	IP	…
148	07/12/13	21:50 – 22:30	S05W26	42.9	B2.2	12	1648	7.3	3.7	IP	…
149	07/12/14	01:30 – 02:00	S09W30	42.9	B9.6	25	36	10.6	6.6	IP	L
150	07/12/14	07:40 – 08:20	S06W31	42.9	B6	12	14	3.9	1.8	I	…

Table 2 (*Continued.*)

No.	Date	Time (UT)	Heliogr. location	Stereo angle (deg)	GOES class	RHESSI[a] E (keV)	RHESSI[a] P (counts s^{-1})	EUVI[b] A (10^5 DN^{-1})	EUVI[b] B	EUVI[b] Com.	CME[c] Rep.
151	07/12/14	08:10 – 08:50	S06W31	42.9	C1.1	12	19	4.2	2.3	I	...
152	07/12/14	14:00 – 14:30	S07W34	43.0	C1.1	12	68	4.4	3.1	IP	...
153	07/12/14	15:10 – 16:20	S05W34	43.0	B8.8	12	432	7.3	4.6	IP	...
154	07/12/15	17:20 – 17:50	S09W51	43.0	B2.8	12	432	6.2	3.6	I	...
155	07/12/16	02:00 – 02:30	S08W56	43.1		12	400	4.5	2.0	I	...
156	07/12/16	03:40 – 04:10	S06W56	43.1	C1.2	12	72	8.9	3.8	IP	...
157	07/12/16	08:30 – 09:00	S07W58	43.1	B1.4	12	288	1.9	0.7	I	...
158	07/12/17	06:40 – 07:30	S09W77	43.1	C2.2	6	96	2.9	3.0	IPO	...
159	07/12/17	20:20 – 20:50	S08W79	43.2	B3.8	12	1392	4.1	1.7	IO	...
160	07/12/17	22:00 – 23:00	S09W79	43.2	B8.9	12	752	3.8	3.2	IPO	L
161	07/12/17	23:30 – 23:59	S09W87	43.2	B5.7	12	368	1.7	0.4	IO	...
162	07/12/18	01:20 – 01:50	S08W80	43.2	B2.4	12	752	8.0	2.3	PO	L
163	07/12/18	04:20 – 04:50	S09W85	43.2	B2.2	12	624	5.2	1.9	IO	L
164	07/12/18	05:10 – 05:40	S08W87	43.2		12	200	0.9	1.3	IPO	...
165	07/12/18	09:30 – 10:00	S08W87	43.2	B2.9	12	848	2.7	0.3	IPO	...
166	07/12/18	09:50 – 10:20	S08W87	43.2	B2.5	12	496	1.2	0.4	PO	L
167	07/12/18	13:00 – 13:30	S07W87	43.2	C2.1	12	80	2.4	0.5	IO	...
168	07/12/18	14:40 – 15:10	S08W87	43.2	C1.1	12	2160	6.4	0.6	IPO	...
169	07/12/18	15:10 – 15:40	S09W87	43.2	B8.4	12	688	8.2	0.6	IPO	...
170	07/12/18	18:50 – 19:30	S18W87	43.2	C1.6	12	80	7.3	0.7	IPO	...
171	07/12/18	22:30 – 23:00	S08W86	43.3	B2.2	12	400	3.1	0.6	IO	L
172	07/12/19	01:30 – 02:00	S08W87	43.3	B2.1	12	272	1.1	0.7	IO	...
173	07/12/19	02:50 – 03:20	S09W87	43.3	B2	12	1072	3.0	1.2	IO	...
174	07/12/30	19:30 – 20:20	S11E87	44.0	C1.7	12	38	0.6	4.2	IO	...
175	07/12/31	00:30 – 01:40	S15E87	44.0	C8.3	25	288	7.5	39.3	IPDOW	LS
176	08/01/01	15:20 – 15:50	S09E72	44.1	C1.1	...	...	3.3	13.6	IO	...

Table 2 (*Continued.*)

No.	Date	Time (UT)	Heliogr. location	Stereo angle (deg)	GOES class	RHESSI[a] E (keV)	RHESSI[a] P (counts s^{-1})	EUVI[b] A (10^5 DN^{-1})	EUVI[b] B	EUVI[b] Com.	CME[c] Rep.
177	08/01/02	08:45 – 11:30	S04E86	44.1	C1.2	12	448	6.1	13.9	IPDO	L
178	08/01/07	14:40 – 16:00	S05W01	44.3	C1.4	12	688	6.2	4.8	I	…
179	08/03/24	02:30 – 03:30	S20E90	47.1	B5.1	12	584	5.5	2.9	IP	…
180	08/03/25	04:30 – 06:30	S10E87	47.1	B4.7	12	848	6.4	8.5	IPO	…
181	08/03/25	14:30 – 15:30	S09E82	47.2	B2.3	12	304	…	4.3	I	…
182	08/03/25	17:30 – 18:00	S06E86	47.2	B2.1	12	272	…	5.4	I	…
183	08/03/25	18:30 – 19:30	S25E90	47.2	M1.7	12	944	17.8	192.2	IPDEW	LS
184	08/04/03	01:00 – 02:00	S12W31	47.7	C1.2	12	32	14.8	11.6	IP	…
185	08/11/04	03:00 – 04:00	N45W45	81.9	C1	12	1712	11.8	4.9	IPD	…

[a]RHESSI:

E = highest detected energy range: 3 – 6, 6 – 12, 12 – 25, 25 – 50, 50 – 100 keV.
P = peak count rate of RHESSI light curve.

[b]EUVI:

A = background-subtracted peak flux detected in STEREO-A/EUVI.
B = background-subtracted peak flux detected in STEREO-B/EUVI.
P = postflare loop emission.
D = dimming in EUV.
E = eruptive feature.
I = impulsive EUV emission.
O = occulted (for A if flare position is east, or for B if west).
T = test images (or poor image quality).
W = waves or oscillations.

[c]CME reports:

L = SOHO/LASCO.
S = SECCHI Cor-1 or Cor-2.

Table 3 Statistics of flare events and types detected with GOES, RHESSI, and STEREO-A/EUVI and STEREO-B/EUVI from 12 December 2006 to 4 November 2008.

Event type	Number	Percentage
Number of cataloged events	185	100%
Number of GOES > C1 events	90	49%
Number of GOES > M1 events	11	5%
Number of RHESSI > 12 keV events	171	92%
Number of CME detections	68	37%
Events with impulsive EUV	147	79%
Events with postflare loops	135	73%
Events with occultation	45	24%
Events with EUV dimming	31	17%
Events with waves or oscillations	10	5%
Events with eruptive features	5	3%

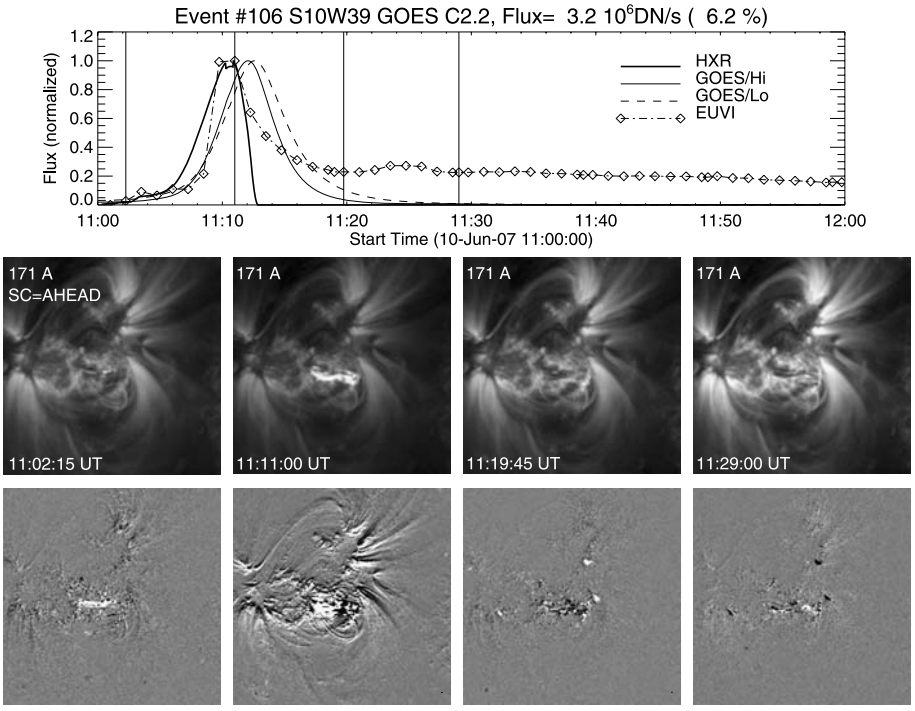

Figure 1 Top: Soft X-ray (GOES/Hi 0.5 – 4 Å and GOES/Lo 1 – 8 Å, thin curves) and EUV (STEREO-A/EUVI, diamonds) light curves, $I(t)$, and time derivative, $dI(t)/dt$, of the harder soft X-ray light curve (thick solid line) for the flare event 106 on 10 June 2007 at 11:10 UT. The preflare-subtracted peak EUVI flux is $F = 3.2 \times 10^6$ DN s^{-1}, which corresponds to 6.2% of the total EUVI flux. Middle: Four STEREO-A/EUVI images, $I(x, y, t_i)$. Bottom: Time difference images, $I(x, y, t_i) - I(x, y, t_{i-1})$. The times (light-travel time corrected) of the EUVI images are marked with diamonds in the top panel, and the times of the selected four images are marked with solid vertical lines. The second selected image at 11:11 UT coincides with the peak of the soft X-ray time derivative.

A new capability of the STEREO mission is the stereoscopic triangulation of flare loops, which we apply here for the first time to flares. We triangulate a few points along the brightest flaring structure (*i.e.*, the brightest structure in the image at 11:11 UT; Figure 1), which is shown enlarged in Figure 2, using the standard stereoscopy code available in the SSW package, as it was first applied to active region loops (Aschwanden *et al.*, 2008a). We find an average altitude of $h = 1.8 \pm 2.4$ Mm (Figure 3), where the uncertainty is largest in the east – west oriented segments of the flaring structure. This horizontally oriented flaring structure, hovering barely over the transition region, appears to be a filament structure, rather than a flare loop or a flare ribbon structure. The MDI magnetogram (Figure 2, bottom) indicates that the filament is located almost parallel to the neutral line, consisting of a highly sheared and horizontally oriented bundle of filament threads. For comparison we also triangulate some 20 active region (AR) loops that surround the flaring structure and find heights up to $h \lesssim 70$ Mm. The full length of the flaring filament structure (see box in Figure 2) is $L_{\rm full} \approx 40$ Mm. Figure 3 shows results of the stereoscopic height measurements of both the primary flaring structure and the 20 AR loops, projected into a direction that shows the AR side-on, to better visualize its vertical structure. Thus, the flaring filament is a low-lying, almost horizontal structure in the core of the active region, with no significant vertical extent, in contrast to typical postflare loops. This is a highly unusual situation that might explain the very impulsive nature of the EUV emission.

To understand the dominance of impulsive EUV emission in this flare we have to investigate the hydrodynamic evolution of an impulsively heated flare loop structure. Using a hydrodynamic model of an impulsively heated loop with subsequent conductive and radiative cooling (with analytical approximations described in Aschwanden, 2009a), we model the light curves observed with the two GOES and the EUVI 171 Å channels. The results are shown in Figure 4. A matching model is found for a uniform heating rate with a peak value of $E_{\rm H} = 20$ erg cm^{-3} and a Gaussian heating time scale of $\tau_{\rm heat} = 120$ s, which matches both the time profiles of the GOES light curves as well as the first impulsive peak in EUVI very closely. A maximum temperature of $T_{\rm m} = 30$ MK is obtained at the time of maximum heating, which drops to $T_{\rm p} \approx 15$ MK at the time of maximum density, which is $n_{\rm p} = 1.4 \times 10^{11}$ cm^{-3}. The peak emission measure is ${\rm EM_p} = 8.83 \times 10^{46}$ cm^{-3} and the flaring filament structure has a half-length of $L = 20$ Mm (according to stereoscopic measurements) and an effective loop width of $w = 500 \pm 200$ km, to match the observed fluxes. Of course, a larger loop diameter is possible with some corresponding filling factor. The conductive cooling time (with $k_{\rm B}$ the Boltzmann constant and $\kappa = 9.2 \times 10^{-7}$ the Spitzer conductivity),

$$\tau_{\rm cond} = \frac{21 n_{\rm e} k_{\rm B} L^2}{5 \kappa T_{\rm e}^{5/2}} \approx 200 \left(\frac{n_{\rm e}}{10^{11}\ {\rm cm}} \right) \left(\frac{L}{10^{9}\ {\rm cm}} \right)^2 \left(\frac{T_{\rm e}}{10^{7}\ {\rm K}} \right)^{-5/2} \quad [{\rm s}], \tag{1}$$

amounts to $\tau_{\rm cond} \approx 429$ s. The radiative cooling time [with a radiative loss function of $\Lambda(T) = \Lambda_0\ T_{\rm e}^{-2/3}$ and $\Lambda_0 = 10^{-17.73}$ in the temperature range of $10^{6.3} \lesssim T_{\rm e} \lesssim 10^{7.0}$],

$$\tau_{\rm rad} = \frac{9 k_{\rm B} T_{\rm e}^{5/3}}{5 n_{\rm e} \Lambda_0} \approx 620 \left(\frac{n_{\rm e}}{10^{11}\ {\rm cm}} \right)^{-1} \left(\frac{T_{\rm e}}{10^{7}\ {\rm K}} \right)^{5/3} \quad [{\rm s}], \tag{2}$$

amounts to $\tau_{\rm rad} \approx 836$ s. Interestingly, the EUVI observations reveal a secondary weaker peak about 14 min ($\approx$840 s) later after the first impulsive peak, associated with the late cooling phase. Therefore, this flare can be understood in terms of an impulsive heating phase that lasts about $2\tau_{\rm heat} \approx 4$ min, as mimicked by the soft X-ray light curves, whereas

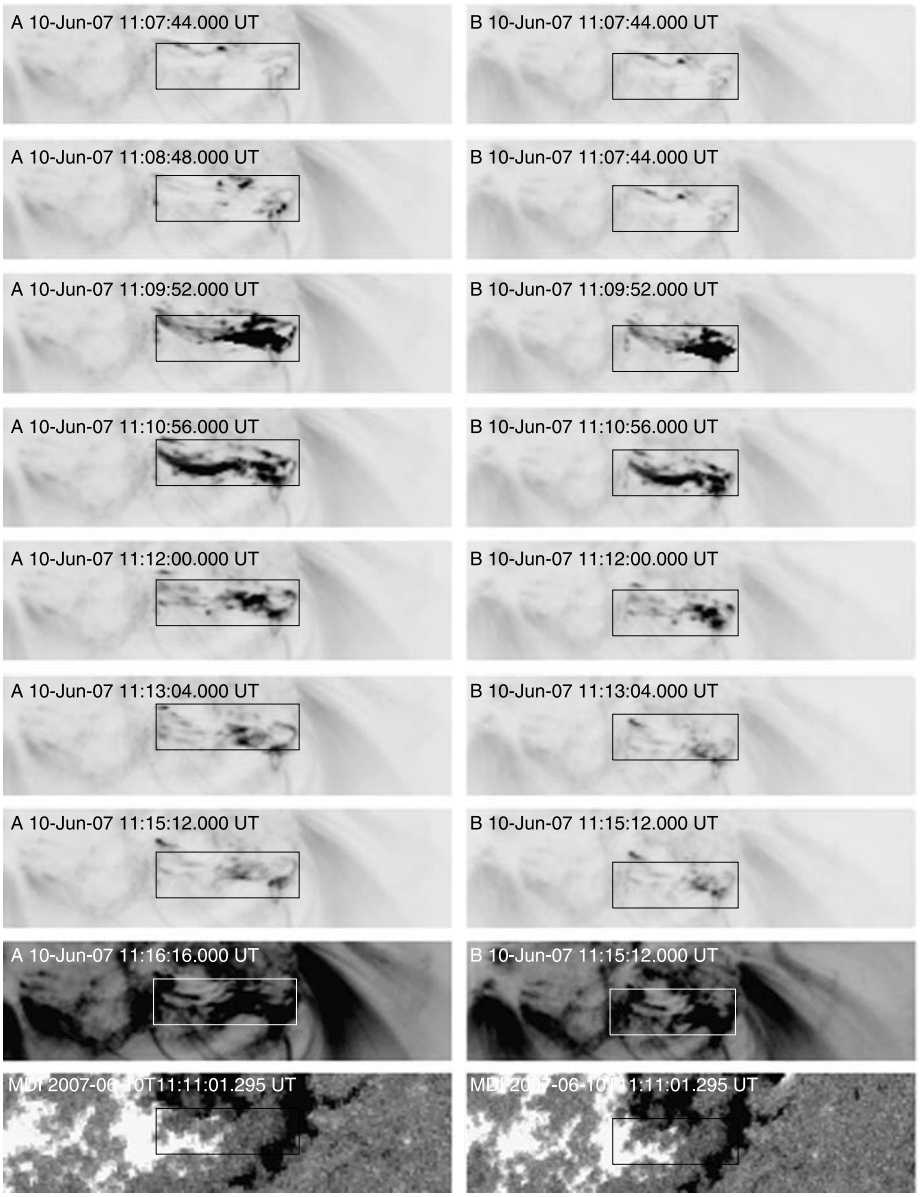

Figure 2 Time sequence of partial images of STEREO-A (left) and STEREO-B (right) for the central flare location of the flare on 10 June 2007 at 11:10 UT. The times indicated are corrected for the light travel time with respect to 1 AU distance from the Sun, and the image frames of B are chosen to be closest to the times of A. The field of view of each partial frame is 180 × 50 EUVI pixels (200 × 60 Mm). The box indicates the location of the brightest filamentary flare structure. The panels in the second row from bottom show the active region with higher contrast. The panels in the bottom row show a coaligned MDI magnetogram, which indicates that the filamentary flare structure straddles along a neutral line from positive (east) to negative (west) magnetic polarity.

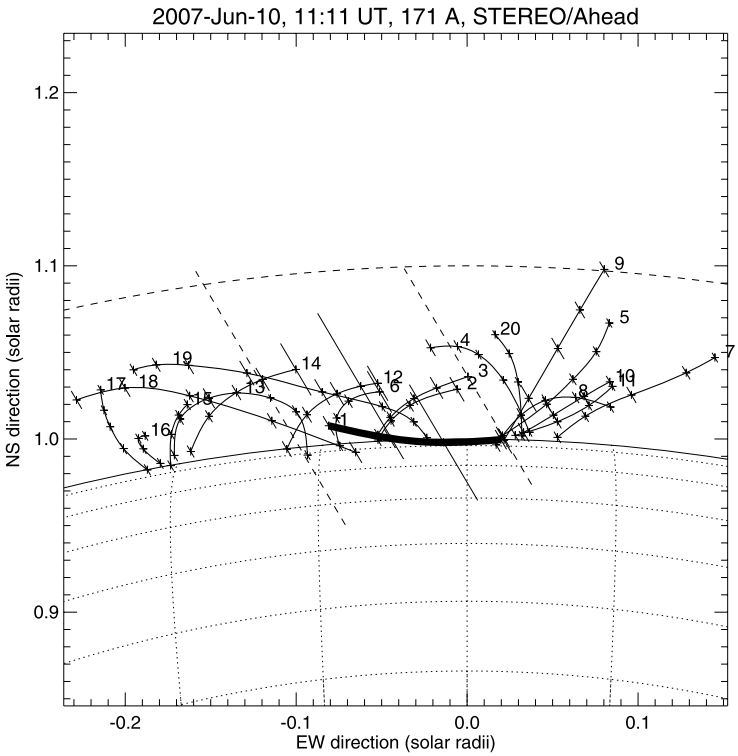

Figure 3 Three-dimensional reconstruction of the flaring filament structure (thick curve) and surrounding active region loops (thin curves) from the STEREO-A/EUVI and STEREO-B/EUVI 171 Å images of 10 June 2007 at 11:11 UT. The error bars are calculated along the line of sight from spacecraft A. The projection of the 3D coordinates is shown from a line of sight that is 30° west from solar disk center and 105° south. Note that the flaring loop structure is just above the solar surface, whereas the surrounding active region loops reach up to heights of $h \lesssim 70$ Mm (dashed line). The coordinate grid has a mesh size of 5° ($\approx$60 Mm) on the solar surface.

the EUVI emission peaks during the initial heating phase and exhibits a secondary peak when the heated flare structure cools through the EUV temperature range. This solution of the hydrodynamic model is not unique, but we could not find another parameter set that fits all three light curves better. Of course, this simple model reproduces the hydrodynamic flare evolution with one single loop only, whereas a multitude of loop strands is expected to be a more realistic approach, which also would improve the fit to the light curves and would constrain filling factors.

What is unique about this flare is the dominance of impulsive EUV emission, with very little EUV emission in the postflare phase. This uniqueness seems to be related to the heating of a noneruptive filament structure that maintains its horizontal structure during the whole flare process. The filament is not erupting, no CME was reported during this flare, and thus it seems to belong into the class of *confined flares*, leaving the overall magnetic structure intact. For comparison, in the Bastille Day 2000 flare it was also found that the impulsive phase of the flare starts with highly sheared, low-lying loop structures located above the neutral line (see Figures 7 and 8 in Aschwanden and Alexander, 2001), whereas the EUV emission later on originated from higher lying postflare loops that formed an arcade between the two chromospheric flare ribbons. We would like to emphasize that this flare is unusual

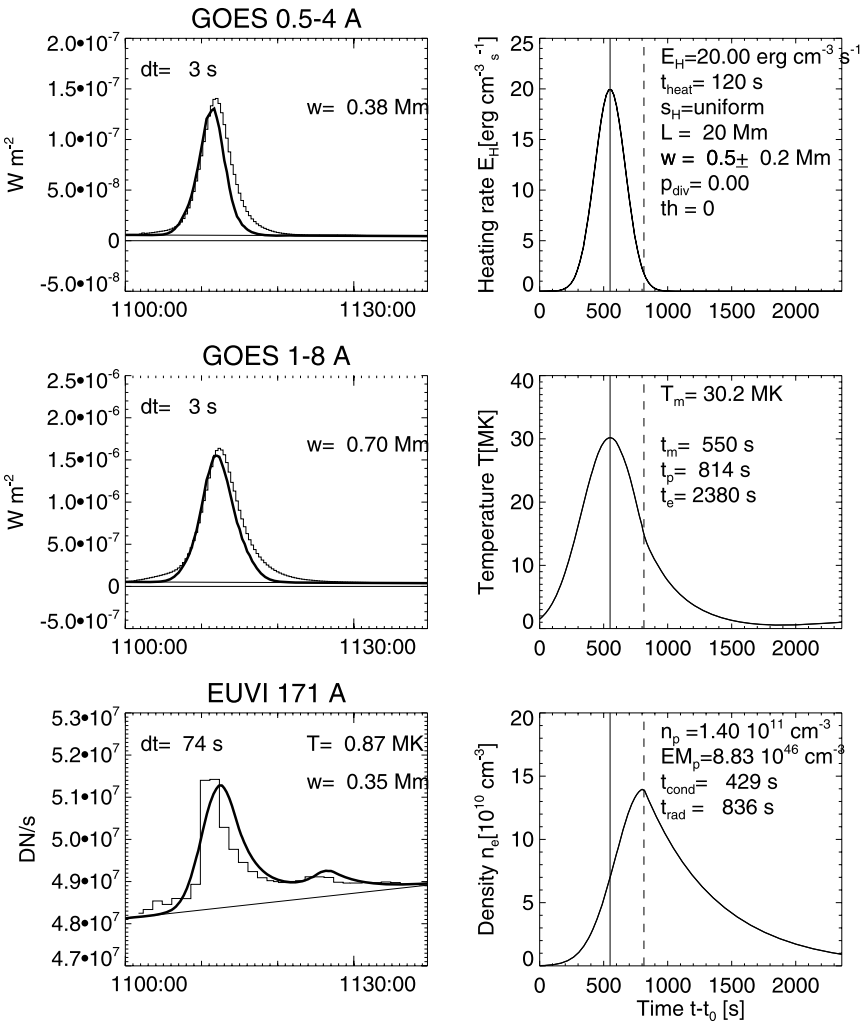

Figure 4 GOES (0.5 – 4 Å, 1 – 8 Å) and EUVI 171 Å light curves (histograms in left panels) of the flare on 7 June 2007, at 11:10 UT, which is also depicted in Figures 1, 2, and 3, fitted with a hydrodynamic model (thick curves in left histograms), calculated based on the heating function $E_{\rm H}(t)$ (top right panel) for uniform heating and a loop half length of $L = 20$ Mm. The resulting temperature profile $T(t)$ (middle right panel) and electron density profile $n_{\rm e}(t)$ (bottom right panel) at the loop apex of this single-loop model are also shown. The values of the widths w have been adjusted to match the observed peak fluxes and differ somewhat in different wavelengths, probably because of temperature-dependent filling factors, obscuration, absorption features, or multiple loop strands.

in the sense that the EUV emission is not dominated by postflare loops of flare ribbons, but rather by a heated, high-density, noneruptive filament.

6. EUV Emission from the Postflare Phase

Most of the EUV emission from flares is generally observed in the postflare phase, after a time delay that corresponds to the cooling time from soft X-ray temperatures

($T \approx 10-30$ MK) down to EUV temperatures ($T \approx 1-2$ MK). Such a typical EUV light curve is shown in Figure 5, for the GOES class M4.5 flare of 3 June 2007, at 06:30 UT, occurring at a heliographic position of S04E63 (event 71 in the flare list in Table 2). The EUV light curve shows first an impulsive peak that roughly coincides with the soft X-ray peak (observed by GOES), within ≈ 1 min; a comparable increase of EUV occurs about 1 hour later, but the soft X rays show no new flaring activity at that time. Such an evolution is quite common, because we observed delayed EUV emission from postflare loops and arcades in $\approx 73\%$ (Table 3) of the 185 flares listed in Table 2.

Let us now examine whether the delayed EUV emission is consistent with cooling of the soft-X-ray-emitting loops that occurred about 1 hour earlier. Shorter cooling times in the order of $\approx 1-30$ min are more common, where the shortest delays result from either conductive cooling of very short loops or from radiative cooling of high-density loops. First we triangulate the postflare loops in question from the stereoscopic images of STEREO-A/EUVI and STEREO-B/EUVI to determine their 3D geometry. We identify eight flare loop segments in both the A and B images that are suitable for triangulation, of which two entail the loop apex. A projection into a horizontal – vertical plane is shown in Figure 6, which shows maximum heights of $h = 46.5 \pm 0.6$ Mm for a complete loop (labeled 1) and $h = 59.2 \pm 1.1$ Mm for a half-loop (labeled 3), respectively. If we take an average loop half-length of $L = h(\pi/2) \approx 80$ Mm, and assume a flare temperature of $T_e \approx 15$ MK and average density of $n_e \approx 0.5 \times 10^{11}$ cm^{-3}, we estimate a conductive cooling time of $\tau_{cond} \approx 40$ min (Equation (1)) and a similar radiative cooling time of $\tau_{rad} \approx 40$ min (Equation (2)), which can quite reasonably explain the observed delay of ≈ 1 hour between the soft X-ray peak and EUV peak (Figure 6, top panel), given the fact that it takes several e-folding cooling times to cool from soft X-ray to EUV temperatures. However, since the conductive cooling time scales quadratically with the loop length, $\tau_{cond} \propto L^2$, all smaller flare loops will cool off earlier and contribute to the slightly enhanced EUV emission that is detected in between the soft X-ray and EUV peak (see the time EUV profile in Figure 5, top panel).

The stereoscopic triangulation enables us to determine the exact length of flare loops in three dimensions, a prerequisite to determine the conductive cooling time τ_{cond} and the total emission measure EM of individual flare loops, which are important parameters for modeling the soft X-ray $I_{SXR}(t)$ and EUV light curves $I_{EUV}(t)$ self-consistently in terms of their hydrodynamic evolution. Studies of multiwavelength light-curve modeling of EUVI and *Hinode* data, using analytical approximations to the hydrodynamic evolution of impulsively heated loops (*e.g.*, the EBTEL code by Klimchuk, Patsourakos, and Cargill, 2008; Raftery *et al.*, 2009), are underway.

7. Occulted Flares

In our survey of 185 flares observed with STEREO we identified 45 events (24%) that were partially or fully occulted for one or both STEREO spacecraft A and B. Because the spacecraft separation angle is less than 90° during the first two years of the mission, flares at the eastern limb can be occulted for the STEREO-A spacecraft, while flares at the western limb can be occulted for the STEREO-B spacecraft. During the beginning of the mission, when the spacecraft had small separation angles (say $\alpha_{sep} \lesssim 10°$, until end of May 2007), a behind-the-limb flare could be partially occulted for both spacecraft.

Occulted flares offer a variety of special diagnostics that cannot be determined with equal accuracy as for disk flares. High-temperature flare loops radiate in the larger apex region in soft X rays, but only the footpoints exhibit a transition to cooler temperatures that contributes

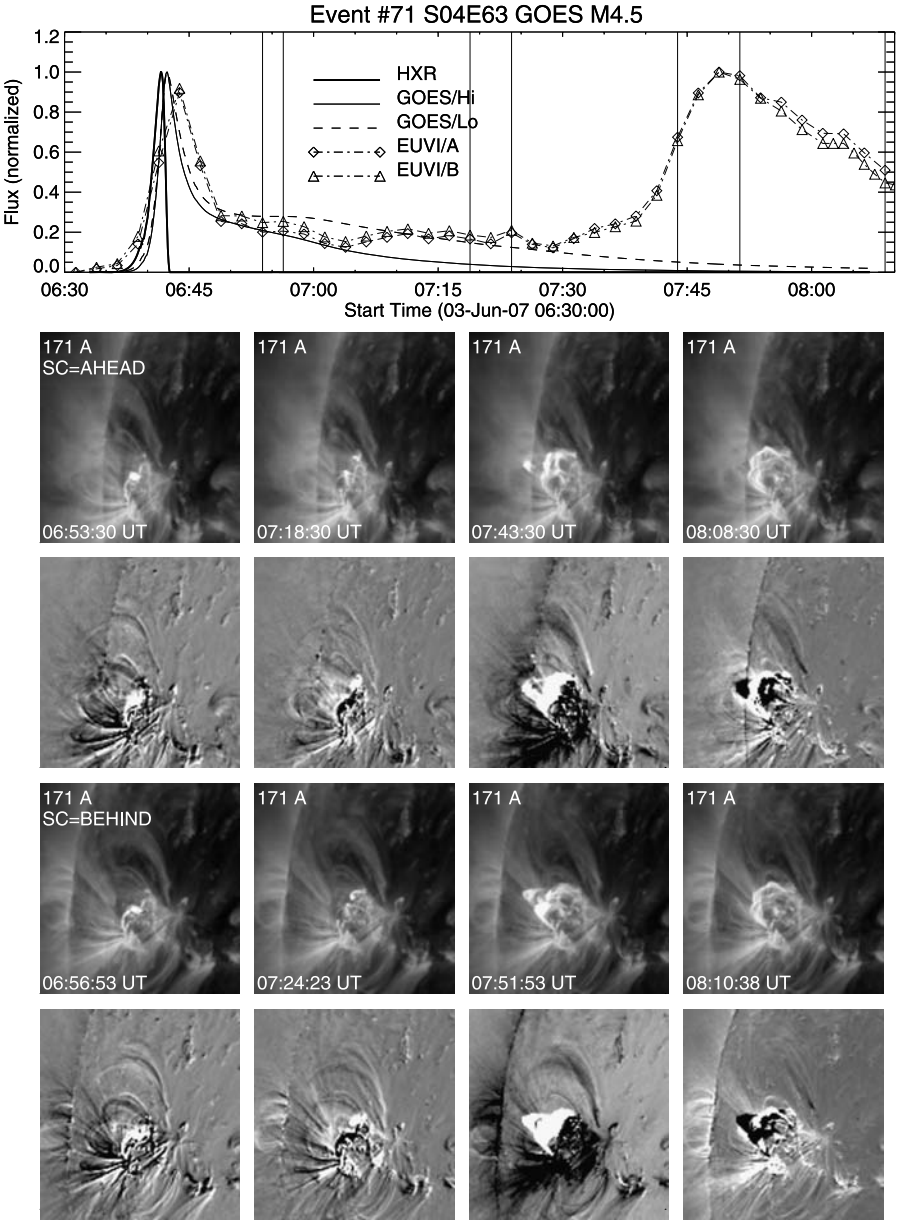

Figure 5 Soft X-ray (GOES/Lo 0.5 – 4 Å and GOES/Hi 1 – 8 Å, thin curves) and EUV (STEREO-A/EUVI and STEREO-B/EUVI, diamonds) light curves, $I(t)$, and time derivative, $dI(t)/dt$, of the harder soft X-ray light curve (thick solid line) for the flare event 71 on 3 June 2007 at 6:30 UT (top panel). The times of EUVI images are marked with diamond and triangle symbols, with the times of the selected images shown below being marked with thick lines. Shown are sequences of four EUVI images (second row) and running-difference images for STEREO-A/EUVI (third row) and STEREO-B/EUVI (fourth an fifth rows, respectively).

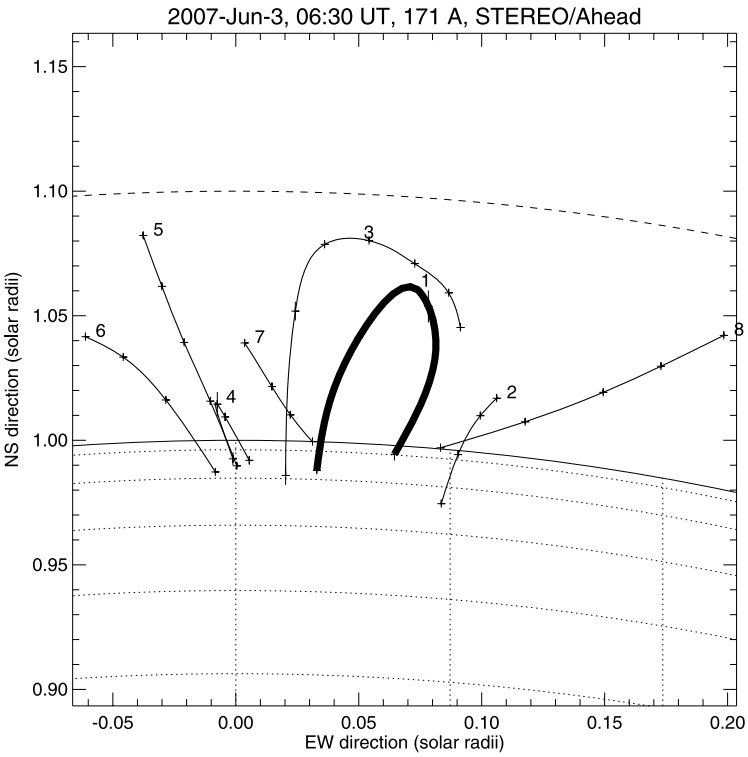

Figure 6 Three-dimensional reconstruction of some postflare loops from the STEREO-A/EUVI and STEREO-B/EUVI 171 Å images of 3 June 2007 at 07:50 UT. The projection of the 3D coordinates is shown from a line of sight that is 20° west from solar disk center and rotated by 90° to solar north. The fully traced central flare loop (thick curve) has a maximum height of $h = 46.5 \pm 0.6$ Mm. The coordinate grid has a mesh size of 5° (≈60 Mm) on the solar surface.

to EUV emission (the so-called moss structure; *e.g.*, Berger *et al.*, 1999). Thus, for behind-the-limb flares that are occulted up to heights of $h \lesssim 5$ Mm, all the bright moss structures are occulted, and no loop-related EUV emission is detectable (although the flare loops are prominently visible in soft X rays), which enables us to measure the uncontaminated EUV dimming in the flare region that is caused by the density rarefication of a launched CME.

Such an example is shown for the flare of 24 January 2007, at 13:30 UT, a GOES-class B9 flare that occurred at S22E89 (event 14 in Table 2). Time profiles of GOES and STEREO-A/EUVI images are shown in Figure 7. Since the two spacecraft A and B had no significant separation at that time, the flare was equally occulted for both spacecraft. The GOES time profile shows a monotonic increase between 13:45 and 14:55 UT, which corresponds to the impulsive flare phase, during which no increase in EUV emission is detected (see the first two images at the time of the steepest soft X-ray increase at 14:15 UT and at the time of the soft X-ray peak at 14:55 UT in Figure 7). In contrast, the total EUV flux (integrated over the image area) decreases abruptly during the rise time of the soft X rays, exhibiting an EUV dimming of -2.2% of the total EUV preflare flux (see the time profile in Figure 7, top panel), which is indicative of coronal mass loss above the flare region. However, after the soft X-ray (1 – 8 Å) peak time of 14:55 UT, the EUV flux starts slowly to rise during the next 5 hours, which is caused by the EUV emission of the postflare loops that slowly rise above

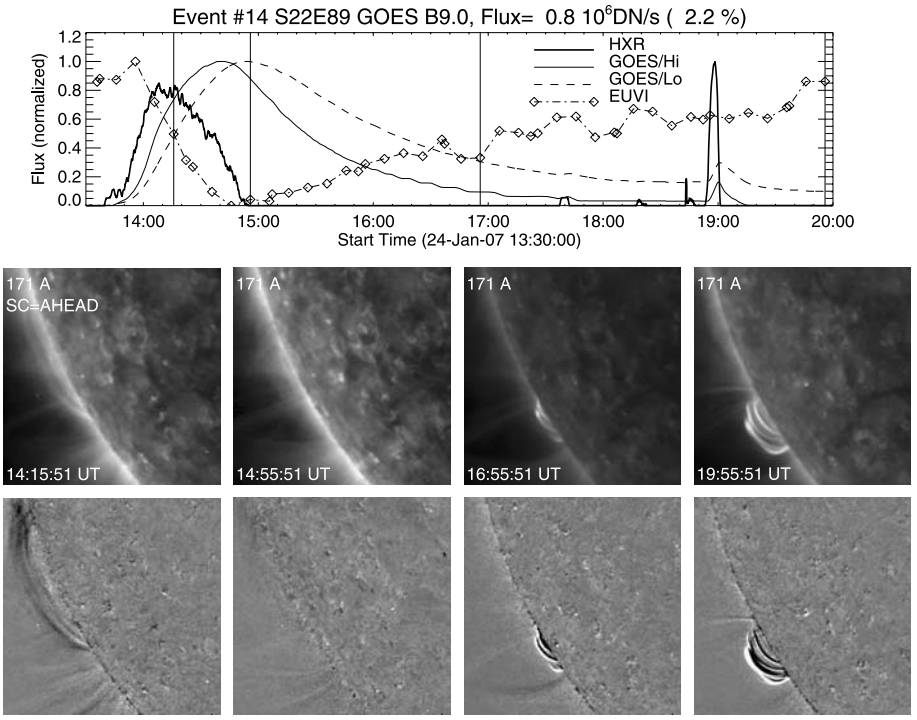

Figure 7 Soft X-ray (GOES/Lo 0.5 – 4 Å and 1 – 8 Å, thin curves) and EUV (STEREO-A/EUVI, diamonds) light curves, $I(t)$, and time derivative, $dI(t)/dt$, of the harder soft X-ray light curve (thick solid line) for the flare event 14 on 24 January 2007 at 13:30 UT (top panel). The maximum of the EUVI light curve has a flux of $F = 0.8 \times 10^6$ DN s^{-1}. The diamond symbols indicate the times of the EUVI images; the vertical lines mark the times of the selected images shown below: four STEREO-A/EUVI images (second row) and running-difference images (bottom row). The gray scales of the EUVI images are adjusted to the maximum brightness in the panels of the middle row.

the limb. The apparent rise of the postflare loops is due to either a vertical expansion of the postflare loops or a vertical progression of the reconnection sites that produce successively higher postflare loops. The solar rotation could also produce (probably a much smaller) increase in the apparent loop height above the horizon, if the flare location is far behind the limb. In any case, this is a clear-cut case when uncontaminated coronal EUV dimming can be measured above a flare region.

With increasing spacecraft separation, the chance for occultation by one spacecraft and nonoccultation by the other becomes more likely, which provides additional information on the vertical structure of EUV emission. In Figure 8 we show the GOES class C8.3 flare of 31 December 2007, at 00:30 UT (event 175 in Table 2), at which time the two STEREO spacecraft had a separation of $\alpha_{\rm sep} = 44.0°$. The flare occurred at a heliographic position of S15E87, and thus it appeared at E65 for STEREO-B and at E109 (or 19° behind the limb) for STEREO-A. Thus, the occultation height,

$$h_{\rm occ} = R_\odot \left(\frac{1}{\cos \Delta l_{\rm limb}} - 1 \right), \tag{3}$$

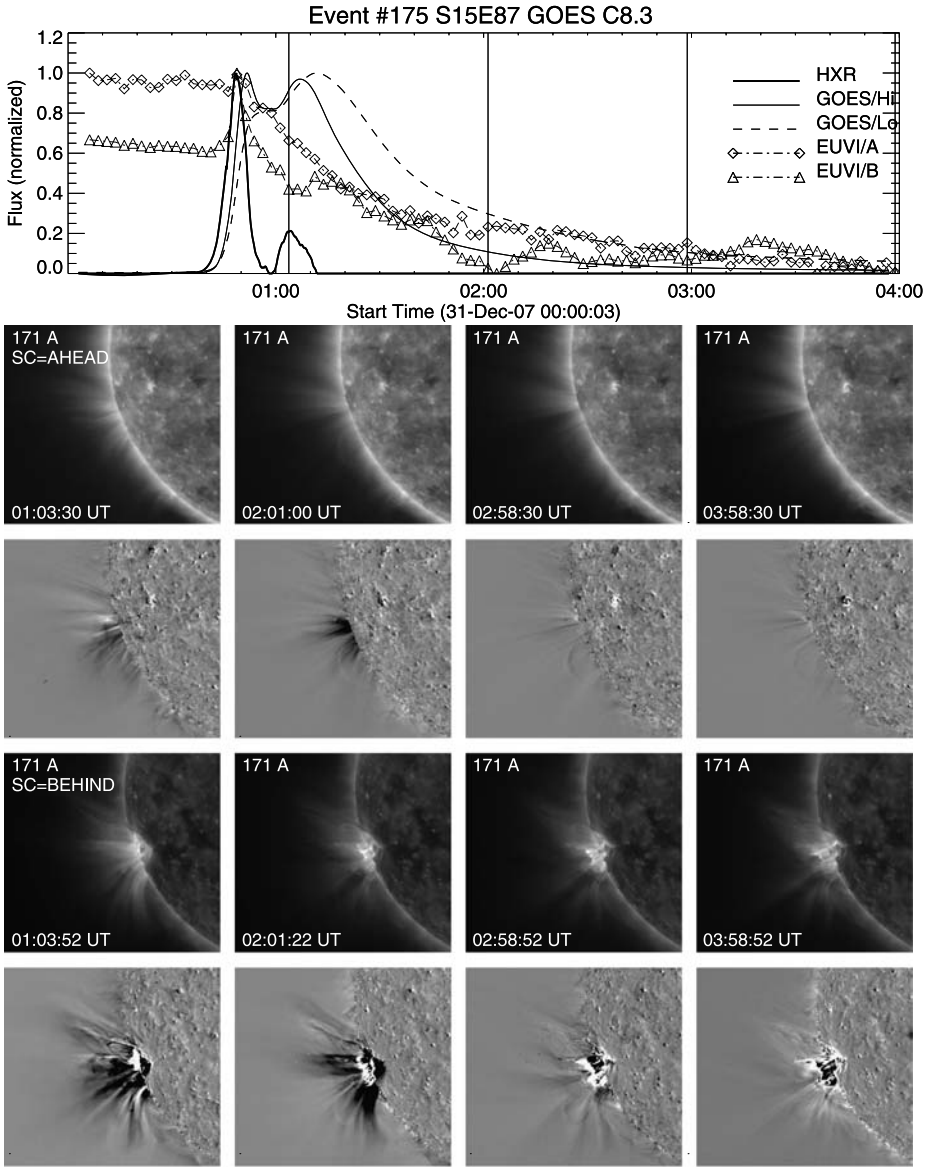

Figure 8 Soft X-ray (GOES/Lo 0.5 – 4 Å and 1 – 8 Å, thin curves) and EUV (STEREO-A/EUVI and STEREO-B/EUVI, diamonds) light curves, $I(t)$, and time derivative, $dI(t)/dt$, of the harder soft X-ray light curve (thick solid line) for the occulted flare event 175 on 31 December 2007 at 00:30 UT (top panel). The diamond and triangle symbols indicate the times of the EUVI images; the vertical lines mark the selected images shown below: sequences of four images (second row) and running-difference images for STEREO-A/EUVI (third row) and STEREO-B/EUVI (fourth and fifth rows, respectively).

for a longitude difference $\Delta l_{\rm limb} = 19^\circ$ behind the limb for STEREO-A is $h_{\rm occ} \approx 40$ Mm. The EUV light curve of STEREO-A/EUVI shows no significant EUV increase during the impulsive flare phase, but only a systematic dimming by -2.9% until about 1 hour after

flare beginning, whereas the light curve of STEREO-B/EUVI shows a prominent impulsive peak of $\approx 4 \times 10^5$ DN s^{-1} (12.3% of the preflare EUV flux), as well as the emission from postflare loops after a delay of ≈ 30 min (Figure 8, top panel). Thus, the EUV dimming seen by STEREO-A/EUVI witnesses the continued mass loss in the wake of the CME, even 1 hour later after flare onset. At the same time, there is no EUV postflare emission above a height of $h \lesssim 40$ Mm even 1 hour after flare beginning, although unocculted soft X-ray emission detected by GOES is substantial (GOES class C8.3 flare). Actually, the GOES soft X-ray flux decays very slowly and returns only after 8 hours to preflare levels. Therefore, this event provides an interesting case to study the evolution of flare heating and associated coronal mass loss in long-duration flares. A more detailed study is underway.

8. CME Expansion and EUV Dimming

EUV observations reveal manifestations of both flares and CMEs. Flares produce EUV emission during the impulsive phase (see Table 3 and Section 5), and more prominently during the postflare phase, when the hot soft X-ray loops cool to coronal temperatures. Since most flares are accompanied by a CME, EUV observations often show the eruption of a cool filament (in absorption on the disk, or in emission above the limb), the compression of plasma at the CME front, and the density rarefication inside the rapidly expanding CME bubble.

A spectacular STEREO observation of this kind is the event of 25 March 2008, at 18:30 UT (event 183 in Table 2). Some images and running-time-difference images of this event are shown in Figure 9, which clearly display the spherically expanding CME bubble during the rise time of soft X-ray emission, which defines the impulsive flare phase. Although soft X-ray emission starts around 18:40 UT and peaks around 18:55 UT, the EUV emission exhibits a dramatic dimming up to -60% (for STEREO-A/EUVI) in the core of the CME bubble during the same time interval (see the time profiles in Figure 9, top panel) for STEREO-A/EUVI. A special feature of this CME is the self-similar expansion of a nearly spherical geometry of the CME bubble. Since this event has been observed with a relatively high cadence of 75 s in 171 Å, we can monitor the CME expansion conveniently.

The EUVI images shown in Figures 9 and 10 clearly demonstrate that the EUV dimming is a direct consequence of the CME expansion. Since the plasma-β parameter is generally assumed to be less than unity in the corona, magnetic forces confine the coronal plasma inside the CME bubble so that it cannot flow across the magnetic field lines that define the boundary of a CME, which appears to have a nearly spherical geometry in this case. We can therefore model the evolution of the average electron density $n_e(t)$ inside the CME bubble with an adiabatic expansion of a sphere with radius $r(t)$,

$$n_e(t) = n_0 \left(\frac{r(t)}{r_0} \right)^{-3}, \tag{4}$$

where $n_0 = n_e(t = t_0)$ and $r_0 = r(t = t_0)$ represent the initial values at the onset of expansion at time $t = t_0$. MHD models of CMEs can compute the time evolution of the driving magnetic forces (*e.g.*, in terms of the Lorentz force or hoop force). If we approximate the driving magnetic force to be nearly constant during some initial time interval, we expect a constant acceleration a, which corresponds to a linear velocity increase $v(t)$ or quadratic radial increase $r(t)$ of the expanding CME bubble,

$$r(t) = r_0 + v_0(t - t_0) + \frac{1}{2} a (t - t_0)^2. \tag{5}$$

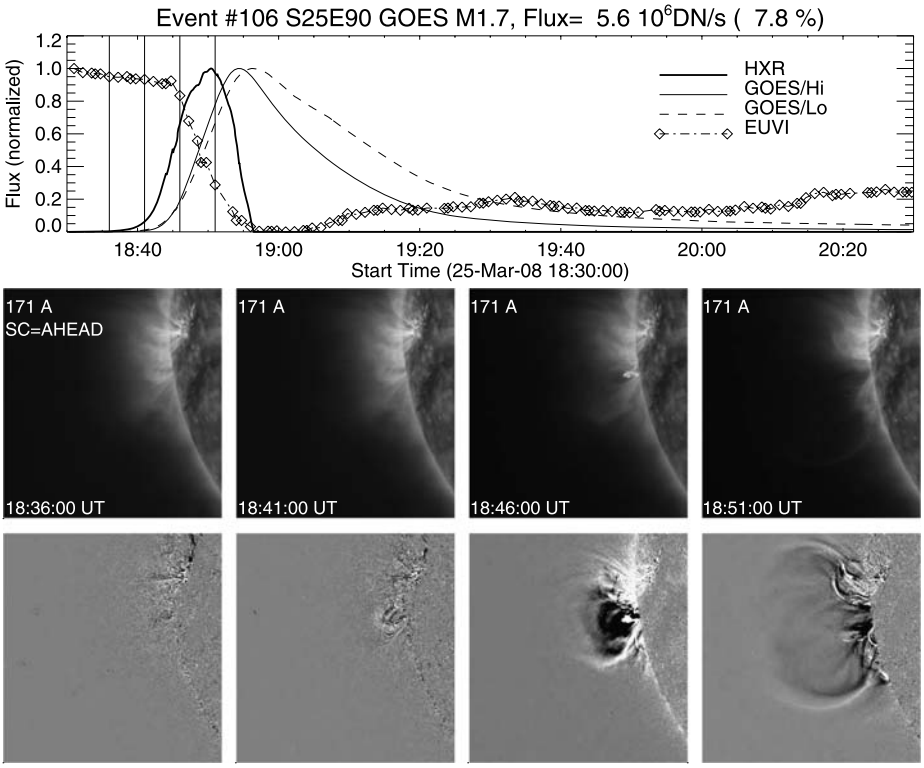

Figure 9 Soft X-ray (GOES/Lo 0.5 – 4 Å and 1 – 8 Å, thin curves) and EUV (STEREO-A/EUVI, diamonds) light curves and time derivative, $dI(t)/dt$, of the harder soft X-ray light curve (thick solid line) for the flare/CME event 183 on 25 March 2008 at 18:30 UT (top panel). Shown are four STEREO-A/EUVI images (second row) and running-difference images (bottom row). Note the strong dimming in the EUV light curve. The diamond symbols mark the times of the EUV images; the selected images shown below are marked with vertical lines. The peak EUV flux is $F = 5.6 \times 10^6$ DN s^{-1} (or 7.8% of the total flux). The field of view of the images is 512 EUVI pixels ($\approx$600 Mm).

Fitting such a quadratic height – time dependence to the radius $r(t)$ of the expanding sphere in Figure 10, we obtain a constant acceleration of $a \approx 0.4$ km s^{-2}, with $r_0 \approx 40$ Mm and $v_0 \approx 0$. This quadratic height – time profile is also indicated in Figure 11.

Modeling the related EUV dimming requires a line-of-sight (LOS) integration of the emission measure EM(x, y, t) for each image pixel location (x, y) along the line of sight z, using a density model $n(x, y, z, t)$ that includes the densities inside the CME bubble as well as in the foreground and background corona,

$$\mathrm{EM}(x, y, t) = \int_{-\infty}^{+\infty} n^2(x, y, z, t)\, dz. \tag{6}$$

The emission measure contribution of the CME bubble rapidly vanishes during the adiabatic expansion. For instance, for a line of sight that intersects the center of the bubble, for a trajectory $x(t) = R_\odot + r(t)$ perpendicular to the LOS, the radius of the CME bubble along

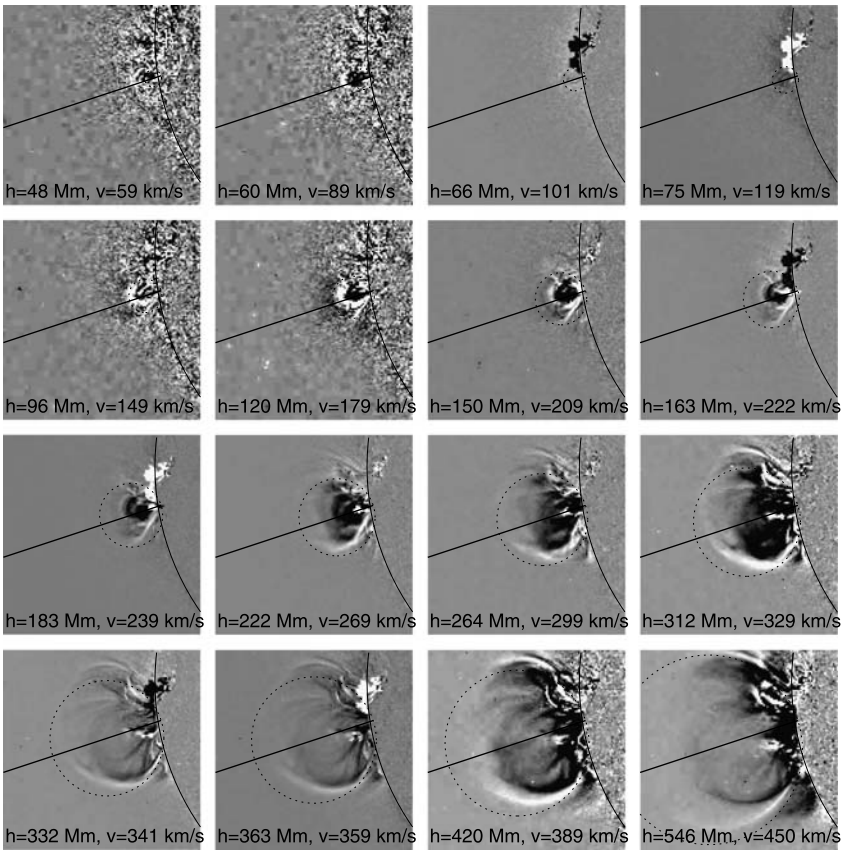

Figure 10 A sequence of 16 running-difference 171 Å images of STEREO-A/EUVI that shows the evolution of the CME expansion during the time interval 18:36 – 18:56 UT on 25 March 2008. A circular geometry (dotted curve) is fitted to the location of the CME front, with the center moving along the vertical direction indicated by a diagonal line. A quadratic fit yields the heights (from $h = 48$ to 769 Mm) and velocities (from $v = 59$ to 540 km s^{-1}) indicated in each panel. The size of the image is $\approx$600 Mm.

the LOS is $z(t) = r(t)$, and we have, with Equations (4) – (6),

$$\mathrm{EM}_{\mathrm{CME}}(t) \propto \int_{-z(t)}^{+z(t)} n_{\mathrm{e}}^2(t)\, dz \propto r(t)^{-5}, \tag{7}$$

so the CME contribution to the EUV flux drops with the fifth power as a function of time, and thus it can readily be neglected in a dimming model. What matters is really the decrease of the emission measure of the foreground and background corona. For the special case of a CME that expands vertically above the limb, as is the case for the 25 March 2008 event, we can assume symmetry for the foreground and background corona. The LOS integration for a hydrostatically stratified background corona then reduces to

$$\mathrm{EM}(x, y, t) = 2 \int_{z_{\mathrm{CME}}(x,y,t)}^{\infty} n_{\mathrm{baro}}^2\big(h[z]\big)\, dz, \tag{8}$$

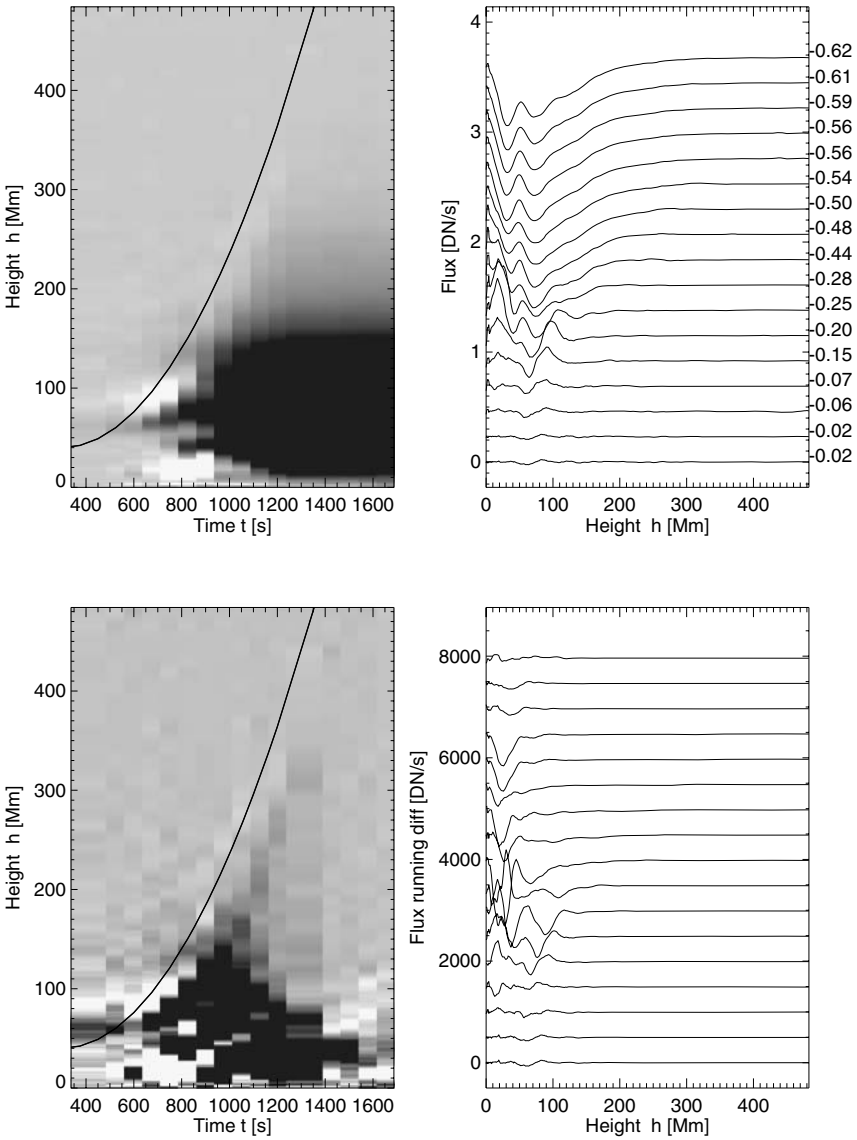

Figure 11 A height – time plot for the (normalized) EUV flux along the vertical trajectory $h(t)$ of the expanding CME, for STEREO-A/EUVI (top) and STEREO-B/EUVI (bottom), in the form of a gray scale (left) and in the form of flux profiles $I_{171}(h,t)/I_{171}(h,t_0)$ (right), normalized to the preflare flux level $I_{171}(h,t_0)$. The flux profiles in the right panels are incrementally shifted as a function of time. Note that the EUV dimming increases from -2% to -62% for STEREO-A/EUVI. The size of the image is ≈ 600 Mm.

where the height $h(z)$ is related to the LOS position z by

$$h(z) = \left(x^2 + y^2 + z^2\right) - R_\odot, \tag{9}$$

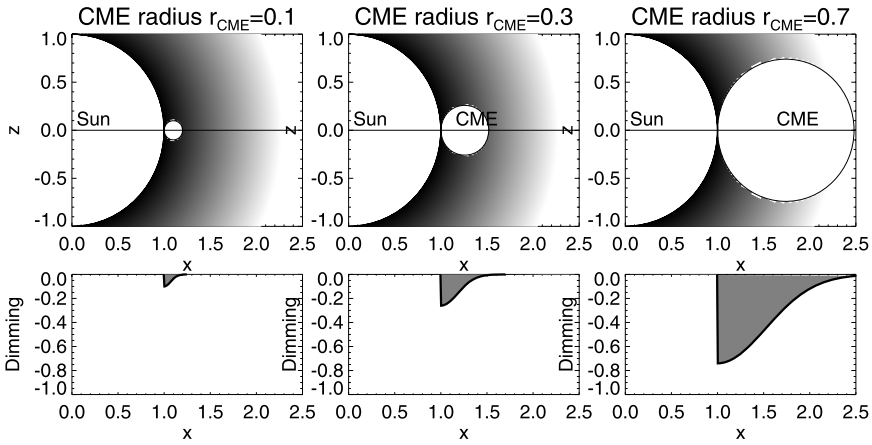

Figure 12 A numerical simulation of adiabatic CME expansion and resulting EUV dimming in the $x-z$ plane for three different times, with x the direction of the CME trajectory and z the line-of-sight direction of the observer. The relative EUV dimming $q_{\rm dimm}(x,t)$ (normalized to the preflare value) resulting from the LOS-integrated emission measure is shown in the lower panels.

$z_{\rm CME}(x,y,t)$ is the LOS extent of the CME at position (x,y) and time t,

$$z_{\rm CME}(x,y,t) = \sqrt{h^2(t) - \left[x - h(t) - R_\odot\right]^2 - y^2}, \tag{10}$$

and $n_{\rm baro}(h)$ is the hydrostatic density model,

$$n_{\rm baro}(h) = n_{\rm base} \exp\left(-\frac{h}{\lambda_T}\right), \tag{11}$$

with λ_T the density scale height of the corona at temperature T. By using these relations (Equations (4)–(11)) it is then straightforward to numerically calculate the resulting EUV flux at a given image position (x,y) for a given EUV filter (say 171 Å), by convolving with the instrumental response function $R(T)$,

$$I_{171}(x,y,t) = \int {\rm EM}(x,y,t,T) R_{171}(T)\, dT, \tag{12}$$

or to quantify the relative dimming $q_{\rm dimm}(x,y,t)$, where the instrumental response function cancels out at a given temperature,

$$q_{\rm dimm}(x,y,t,T) = \frac{I_{171}(x,y,t)}{I_{171}(x,y,t_0)} = \frac{{\rm EM}(x,y,t,T)}{{\rm EM}(x,y,t_0,T)}. \tag{13}$$

However, since the density scale height λ_T depends on the temperature, the relative EUV dimming will still have some temperature dependence. The observed dimming profiles $q_{\rm dimm}(h,t)$ are shown in Figure 11 (right panels) and can directly be fitted with Equation (13) at the lower envelope to constrain the parameters of the coronal base density $n_{\rm base}$ and the kinematic CME parameters h_0, v_0, and a. A numerical simulation of our density model and resulting EUV dimming caused by adiabatic expansion is shown in Figure 12 (for three instants of time).

More comprehensive modeling of EUV dimming will be presented in a separate study (Aschwanden *et al.*, 2009b). Detailed quantitative modeling of EUV dimming will not only establish the intimate connection between EUV dimming and CME expansion but also provide an accurate method to determine the CME kinematics right at the origin, which can then be cross-compared with MHD models. It is hoped that such kinematic comparisons will help to discriminate the CME driving forces in different 3D MHD models (*e.g.*, Chapter 17 in Aschwanden, 2004), such as: (1) the disruption of a global-scale streamer (*e.g.*, Illing and Hundhausen, 1986; Steinolfson and Hundhausen, 1988), which reproduces the observed three-part structure with a bright front, a dark cavity, and a bright core containing the helical prominence or filament, (2) the magnetic buoyancy force that drives the outward motion (*e.g.*, Yeh and Wu, 1991; Wu and Guo, 1997); (3) emerging flux that drives the CME eruption (*e.g.*, Chen and Shibata, 2000); (4) shearing of magnetic footpoints (*e.g.*, Linker and Mikic, 1995; Mikic and Linker, 1994); (5) the torus flux rope model (*e.g.*, Chen, 1997; Chen *et al.*, 2000; Krall, Chen, and Santoro, 2000); (6) the kink instability flux rope model (*e.g.*, Fan and Gibson, 2003, 2004; Török and Kliem, 2003; Török, Kliem, and Titov, 2003; Kliem, Titov, and Török, 2004); or (7) a combination of photospheric shearing and opposite-polarity emergence that produces erupting twisted magnetic flux ropes (*e.g.*, Amari *et al.* 2000, 2003a, 2003b).

9. CME Mass Determination with EUVI

The mass of CMEs is usually estimated from the ratio of the excess observed brightness $I_{\rm obs}$ (from difference images) to the brightness $I_{\rm e}(\vartheta)$ of a single electron at angle ϑ from the plane of the sky, which is computed from the Thomson scattering function (Billings, 1966). If one assumes a standard abundance in fully ionized hydrogen with 10% helium (*i.e.*, a mean molecular mass of $\mu = 1.27$), the relation for the CME mass is then

$$m_{\rm CME} = \frac{I_{\rm obs}}{I_{\rm e}(\vartheta)} \mu m_{\rm p} \approx \frac{I_{\rm obs}}{I_{\rm e}(\vartheta)}\, 2 \times 10^{-24} \quad [{\rm g}]. \tag{14}$$

Typical CME mass estimates are in the order of $m_{\rm CME} \approx 10^{14} - 10^{16}$ g. A refined methodology of proper treatment of the Thomson-scattered emission can be found in Vourlidas and Howard (2008).

To our knowledge there are no reports of CME masses based on EUV observations, in particular in terms of the EUV dimming. There is a statistical study that investigated the relationship between EUV dimming (detected with SOHO/CDS) and CME events (detected with LASCO) for the time span of 1998 – 2005, showing that 55% of identified dimming regions are associated with CMEs, while 84% of the detected CMEs could be tracked back to dimming regions (Bewsher, Harrison, and Brown, 2008). So, there is an intimate relation between the launch of a CME and the resulting EUV dimming of the solar corona. On physical grounds we expect that the EUV dimming should scale directly with the mass and volume of the CME, because the EUV dimming is simply the subtraction of the EUV emission of the CME plasma from the pre-CME corona. If we approximate the volume $V_{\rm CME}$ of a CME with a quadratic footpoint area of length $l_{\rm CME} = R_\odot \theta$ (where θ is the latitude or longitude extent in radians) and a height of a hydrodynamic density scale height λ_T, we have

$$V_{\rm CME} = (R_\odot \theta)^2 \lambda_T, \tag{15}$$

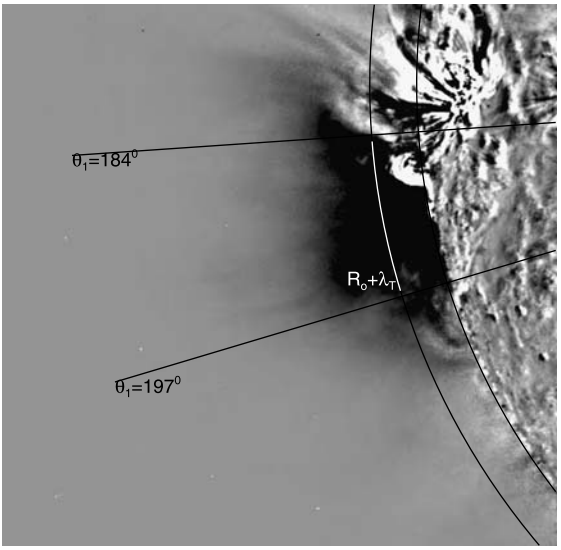

Figure 13 A difference image for the flare of 25 March 2008 in which the pre-flare image at 18:31 UT is subtracted from the after-flare image at 19:29 UT to visualize the total amount of coronal dimming. The dimming region is confined to the position angle range of 184° – 197°, which yields an opening angle of $\Delta\theta = \theta_2 - \theta_1 \approx 13°$. Also indicated is the coronal altitude of one density scale height $\lambda_T = 47$ Mm for a temperature of $T = 1.0$ MK, which approximately defines the altitude range of the CME mass loss.

which leads to the following CME mass estimate:

$$m_{\rm CME} = V_{\rm CME} n_{\rm e} m_{\rm p} = 1.16 \times 10^{15} \left(\frac{\theta}{10°}\right)^2 \left(\frac{T}{1\ {\rm MK}}\right) \left(\frac{n_{\rm base}}{10^9\ {\rm cm}^{-3}}\right) \quad [{\rm g}]. \qquad (16)$$

For a typical base density of $n_{\rm base} = 10^9$ cm^{-3}, a coronal temperature of $T = 1.0$ MK, and an opening angle range of $\theta \approx 3° - 30°$, this yields CME masses in the range of $m_{\rm CME} \approx 10^{14} - 10^{16}$ g. More accurate estimates could easily be obtained be combining the three coronal EUV filters (171, 195, and 284 Å), to have a more comprehensive temperature range (*i.e.*, $T \approx 0.7 - 2.7$ MK for these filters).

Applying relation (16) to the 25 March 2008 flare, where the EUV dimming extends over an opening angle of $\theta \approx 13°$ (Figure 13), we estimate a CME mass of $m_{\rm CME} \approx 2 \times 10^{15}$ g, which includes the CME plasma in the temperature range of $T \approx 0.7 - 1.3$ MK, and thus represents a lower limit for the entire CME mass. In future investigations we plan to combine multiple temperature filters and to model the coronal densities involved in the EUV dimming (Equation (13)) and in the CME mass (Equation (16)) in a self-consistent manner.

10. Erupting Filaments

Because CMEs generally have the three-part structure with a bright front, a dark cavity, and a bright core containing the helical prominence or filament, we would expect to observe with EUVI an eruptive filament for each CME event. Our initial survey, however, reveals a much smaller number (*i.e.*, about five cases with eruptive features, out of 68 flare events when a CME was reported within about an hour), according to the statistics in Table 3. Part of this discrepancy might come from false associations of flare events with reported CMEs (since we used only the temporal coincidence without scrutinizing the co-spatiality in LASCO or SECCHI/Cor-1 and Cor-2 movies, a task for a future study), from insufficient EUVI cadence, from confusion of small-scale structures (*i.e.*, filamentary threads are hard

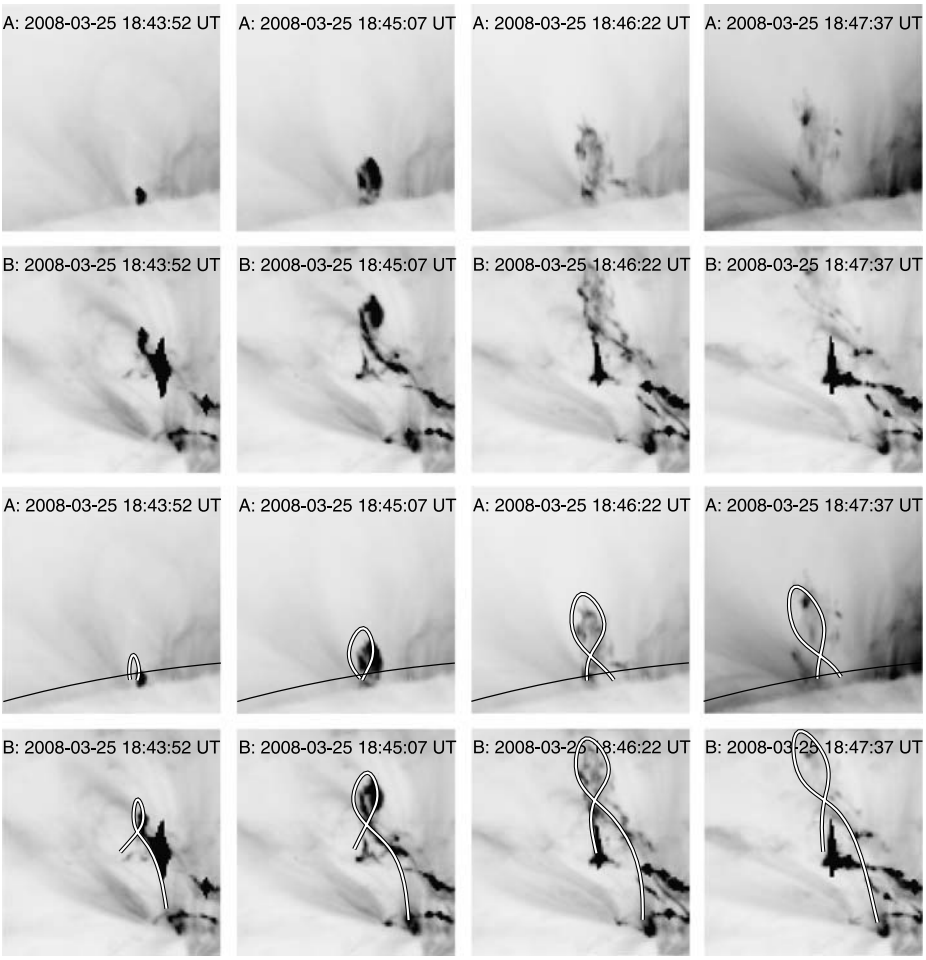

Figure 14 The eruptive filament in the core of the flare/CME event of 25 March 2008 at 18:43:52 UT. Four EUVI 171 Å images are shown for A, for which the lower part of the filament is occulted (top row), and for B, which shows the filament in full view (second row). The topology of a twisted flux rope is overlayed onto the same images (third and fourth rows). The images are rotated by 90° to visualize the vertical orientation. The size of each image frame is 100 EUVI pixels (120 Mm).

to discriminate from underlying moss structure), or just from insufficient flux sensitivity. Especially the time cadence is crucial, since an eruptive filament expands and breaks up into faint filamentary threads within a few minutes. In addition, since an erupting filament expands rapidly in volume, the emission per volume element quickly fades and becomes undetectable. Nevertheless, although we have not yet tackled a systematic search of eruptive filaments, there must exist many more events in the EUVI database.

An example of an eruptive filament is shown for the flare/CME event of 25 March 2008, at 18:30 UT (event 183 of Table 2). The relative size of the tiny filament structure compared with the much larger size of the CME bubble can be seen in the time sequence of difference images shown in Figure 10. The evolution of the eruptive filament is detectable during a time interval of about 6 min (18:42 – 18:48 UT), of which we show four frames in Figure 14

(from 18:43:52 to 18:47:37 UT), when EUVI had a basic cadence of 75 s. STEREO-B/EUVI sees the eruptive filament in full view, while STEREO-A/EUVI sees the lower part of the filament occulted. STEREO-B/EUVI also exhibits saturation in some parts of the filament, which hampers the reconstruction of some details. Overall, the images suggest a twisted flux rope with at least one helical turn, which breaks up into multiple helical strands during the eruption, especially evident in the frame of 18:46:22 UT. At this point, this topology could be consistent with several MHD models, such as the kink-unstable flux rope model (*e.g.*, Fan and Gibson, 2003, 2004; Török and Kliem, 2003; Török, Kliem, and Titov, 2003; Kliem, Titov, and Török, 2004) or the sheared and opposite-polarity emerging twisted magnetic flux rope model (*e.g.*, Amari *et al.* 2000, 2003a, 2003b). A more detailed 3D reconstruction of this eruptive filament requires some dynamical modeling. Stereoscopic triangulation can pin down the exact 3D trajectory, mostly the coordinate along the line of sight, while the vertical coordinates are already well constrained from the images (since the eruption occurs near the limb). Also, examination at other wavelengths may fill in some additional details of the 3D topology, although the lower cadence (by about a factor of about 5) in 195 and 284 Å provides only one single image during the eruptive phase. This example demonstrates the demand for high-resolution, high-cadence, and high-sensitivity observations that is needed for the detailed 3D reconstruction of an eruptive filament, but it is hoped that larger CME events in the near future will provide more massive and voluminous eruptive filaments.

11. Coronal Loop Oscillations and Waves

The 10 events containing some wave and oscillation phenomena listed in Table 2 are only a lower limit, since we have not yet performed a systematic search of oscillatory features through the entire EUVI database. At the time of this writing, there exist clear indications of more such events. For instance, a search of EIT wave events during the STEREO epoch revealed some 34 candidates, of which 7 events have been studied so far (David Long, presentation at SECCHI consortium meeting, October 2008). One event with AR loop kink-mode oscillations, already the subject of a detailed study (Verwichte *et al.*, 2009; Aschwanden, 2009b), will briefly be described in the following. In general, it is expected that during their vertical expansion most CMEs produce a lateral pressure disturbance in the ambient plasma that displaces AR loops. If this disturbance is sufficiently fast, AR loops overshoot their new equilibrium position and undergo a strongly damped kink-mode oscillation. The details of this excitation model, however, are still largely unexplored. Sometimes, loop oscillations are observed in association with a flare, but without a reported CME, as is the case in the event analyzed in this section. Nevertheless, the occurrence of a CME or eruptive filament provides a good guide in the detection of loop oscillations, as was already noticed in early TRACE observations (*e.g.*, Schrijver *et al.*, 1999; Schrijver, Aschwanden, and Title, 2002). Hence, a systematic search for AR loop oscillations, as well as for EIT-type waves, should focus on the time interval of about 1 hour after the onset of flares and CMEs.

The flare/CME event of 27 June 2007 at 17:30 UT (event 109 in Table 2) occurs at the eastern limb (S20E89). It displays a compact small flare (GOES C1.3 class) with an impulsive EUV brightening around 18:00 UT (Figure 15, top frame), after which a connected large-scale loop to the south starts to oscillate. The oscillation is best visible in movies, but it can also be gleaned from a sequence of running-difference images during 17:58 and 18:26 UT (Figure 16), where the bright rim of the loop indicates its new position and the black rim its previous position. There are indications that the oscillating loop

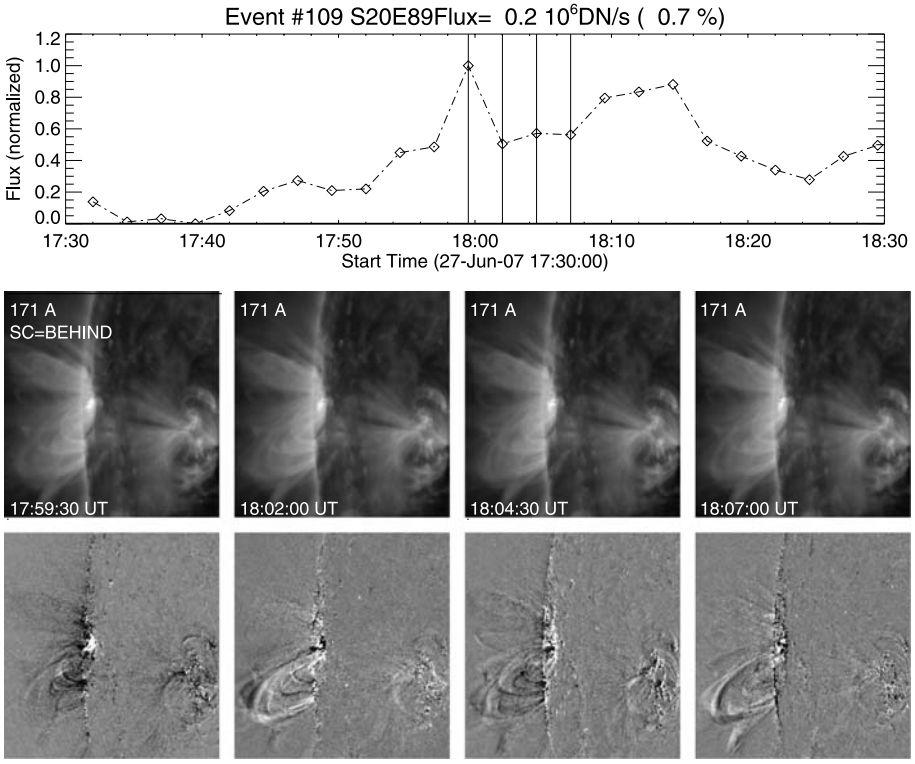

Figure 15 The STEREO-B/EUVI total flux (top), images (second row), and running-difference images (third row) of the flare/CME event on 27 June 2007 at 17:30 UT (event 109 in Table 2). The maximum EUV flux is $F = 0.2 \times 10^6$ DN s^{-1} (*i.e.*, 0.7% of the total EUV flux). The diamonds mark the times of the EUVI images; the times of the four selected images shown below are marked with vertical lines. Note a compact flare that causes a peak in the EUV time profile at 18:00 UT, after which a connected large-scale AR loop in the south begins to oscillate.

consists of multiple strands that are not fully resolved with EUVI, which makes it difficult to carry out an accurate stereoscopic triangulation. Nevertheless, it can clearly be measured that this loop undergoes transverse kink-mode oscillations (Aschwanden *et al.*, 1999; Nakariakov *et al.*, 1999), which are strongly damped. Our EUV cadence is 150 s here. We fit the amplitude transverse to the loop axis (at a position indicated in Figure 16) using

$$a(t) = a_0 + a_1 \cos\left(\frac{2\pi(t - t_0)}{P} + \Phi\right) \exp\left(-\frac{t - t_0}{\tau_d}\right) \tag{17}$$

and obtain an initial amplitude of $a_1 = 2.5$ EUVI pixels (2900 km), a period of $P = 565$ s (≈ 9 min), and an exponential damping time of $\tau_d = 1600$ s (≈ 27 min). Commensurable values were measured at a different loop position in the study of Verwichte *et al.* (2009). Because we can only measure about 2 or 3 periods (Figure 17), the uncertainty of periods and damping times strongly depends on spatial gradients of the underlying time-variable background, and thus on the loop location of the measurement. The 3D loop geometry was also modeled in Verwichte *et al.* (2009), which allows us then (using also a density determination) to estimate the magnetic field in the loop and ambient corona.

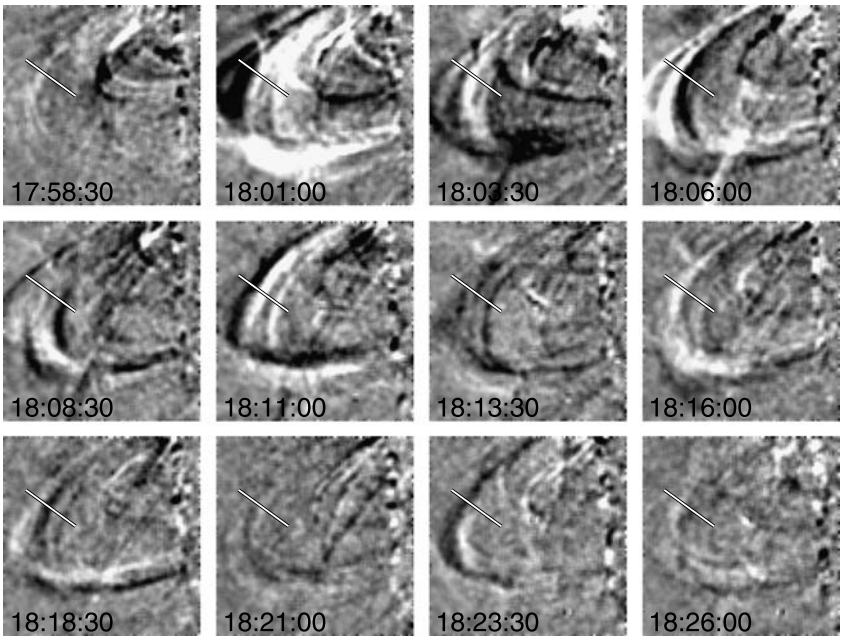

Figure 16 Sequence of running-difference STEREO-B/EUVI images in the area of the oscillating loop during the time period of 17:56:00 and 18:26:00 UT on 26 June 2007. The amplitude measurement of the oscillating loop is carried out along the cross-sectional slit marked with a diagonal bar.

This case is the first loop oscillation event analyzed from STEREO/EUVI and has the potential to provide true 3D coordinates of oscillating loops (Aschwanden, 2009b). If we manage to separate the oscillating loop structure cleanly from the time-variable background, we can potentially measure the 3D coordinates of the oscillating loop, which will allow us to discriminate vertically from horizontally polarized transverse kink modes, combinations of kink modes and torsional modes, fundamental and harmonic modes, or standing and propagating waves. There is a good chance that we will be able to isolate oscillating loops from the background, because the two spacecraft provide redundant information on the loop density and cross section. A limitation of the EUVI data is the cadence, which is typically 150 s in 171 Å (or 75 s in the best case), which puts a lower limit of $P \gtrsim 5$ min (or 2.5 min) on the detection of kink-mode periods. Another difficulty is tracking the identity of an oscillating loop during a flare episode, since the radiative cooling time of typical AR loops at $T \approx 1.0$ MK is about $\tau_{\rm cool} = 17 \pm 7$ min, as was measured in oscillating loops (Aschwanden and Terradas, 2008), using a higher spatial resolution (with TRACE) than EUVI. Thus the hydrodynamic evolution has to be considered in the stereoscopic reconstruction of oscillating loops.

12. Conclusions

This study contains a preliminary survey of flare and CME observations by EUVI during the first two years of the STEREO mission. The purpose of this survey is to provide a comprehensive list of events that merit a more detailed analysis, to demonstrate in a few examples what quantitative measurements are feasible with EUVI data, and to highlight

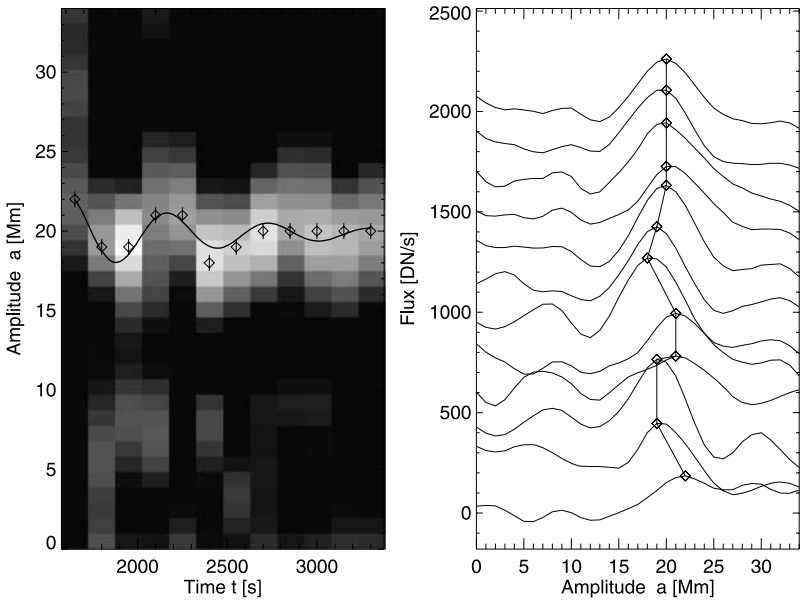

Figure 17 Cross-sectional profile $F(a)$ that shows the transverse loop motion as a function of the perpendicular distance a (right), and the oscillatory amplitude as a function of time (left). A damped oscillation curve is fitted (thick black curve). See fit parameters in text.

what scientific questions can be addressed with stereoscopic 3D reconstructions. From this survey we draw the following conclusions:

1. Despite the paucity of larger flare and CME events in the minimum of the solar cycle during the first two years of the STEREO mission, there occurred a host of small flares of GOES classes B, C, and M that provide significant information on the hydrodynamics of flares and the kinematics of CMEs. Although we selected events from soft X rays ($>$ C1 class) and hard X-ray ($>$ 25 keV) flare catalogs, we detected in each of the 185 selected events significant EUV emission in the STEREO-A/EUVI and STEREO-B/EUVI images, each one displaying a unique evolution that is suitable for hydrodynamic modeling. This dataset covers also a unique phase (of the first two years) of the STEREO mission when small- and moderate-angle stereoscopy (with spacecraft separation angles of $\lesssim 90°$) is facilitated.
2. EUV emission (at $T \approx 1.0$ MK) during flares/CMEs exhibit at least three different components in their time evolution: (1) impulsive EUV emission that peaks simultaneously with hard X rays (or the time derivative of the soft X rays, according to the Neupert effect), (2) postflare emission that occurs with a delay of ≈ 10 min to 1 hour and is caused by the postflare loops (and arcades) that cool from their initial soft X-ray temperature to the EUV temperature regime, and (3) EUV dimming that is caused by the evacuation of plasma during the initial expansion of CMEs. A new result that is derived here with stereoscopic measurements is that the impulsive EUV emission from a low-lying, horizontally oriented filament can dominate in the impulsive phase. The density of this filament is sufficiently high to cause a very short radiative cooling time, so that the EUV emission during the impulsive flare phase dominates over the postflare EUV emission. Stereoscopic 3D reconstructions of flares provide the loop length and inclination angle

of postflare loops, which are prerequisites for a determination of the conductive cooling time and proper hydrodynamic modeling.

3. Occulted flares, of which we identified some 45 events, provide special information that can be exploited for modeling: (1) Slightly occulted flares show most of the soft X-ray emission (in loop apex regions) but hide the EUV emission (from the footpoints or moss regions of hot loops) and in this way display the uncontaminated EUV dimming in the flare/CME region. Uncontaminated EUV dimming measurements allow us to model the initial expansion of CMEs. (2) Slightly occulted flares also show coronal hard X-ray emission (of the Masuda type), which is one of the most direct diagnostics of the primary acceleration region, while the bright thick-target bremsstrahlung emission from the footpoints is eclipsed, and thus provides the necessary contrast to map the faint coronal emission (*e.g.*, Krucker and Lin, 2008). This is a particularly interesting opportunity for combined RHESSI and STEREO/EUVI data analysis.
4. EUV dimming indicates a transient deficit of expected EUV emission below the level of the background corona or AR, which appears clearly to be associated with the initial expansion of a CME. We demonstrated how the spatio-temporal measurements of EUV dimming can be processed to model the initial expansion of a CME. The results of this type of stereoscopy-aided modeling yields the 3D kinematics of the CME, which can be compared with numerical simulations of full MHD models to discriminate among different theoretical models of the driving force of CMEs. Moreover, 3D modeling of EUV dimming also provides a direct method to estimate the mass of a CME in the lower corona, which complements mass estimates from white-light data (Cor-1 and Cor-2) obtained in the outer corona.
5. Three-dimensional reconstructions of eruptive filaments provide the kinematics in the core of an expanding CME, which can also be compared with numerical simulations of MHD models to identify the driving forces directly above the neutral line.
6. The rapid expansion of a CME exerts a lateral Lorentz force to the ambient plasma outside the CME bubble, which displaces AR loops and can excite kink-mode oscillations. The 3D modeling of oscillating loops contains interesting physics in its own right, allowing us for the first time to properly discriminate vertically from horizontally polarized transverse kink modes, to disentangle kink modes from torsional modes, to identify fundamental and harmonic modes, or to discriminate standing from propagating waves.
7. The onset of a CME is often also accompanied by generation of Moreton waves, EIT waves, or global waves. The 3D modeling of these global waves detectable in EUV is likely to give us new insights into their physical nature, because we should be able to constrain the altitude in which they propagate, and thus can better determine the densities, magnetic fields, and Alfvén speeds that are necessary to identify their magnetoacoustic mode.

There is clearly a lot of exciting new scientific potential in stereoscopic EUV data, which we have outlined (rather superficially) in this article. For most of the scientific issues that can be addressed with 3D reconstruction methods of EUV emission in the lower corona, the dataset appraised in this survey is our only chance in the near future to benefit from classical (small- to moderate-angle) stereoscopy.

Acknowledgements We thank the anonymous referee for constructive and helpful comments. This work is supported by the NASA STEREO mission under NRL Contract No. N00173-02-C-2035. The STEREO/SECCHI data used here are produced by an international consortium of the Naval Research Laboratory (USA), Lockheed Martin Solar and Astrophysics Lab (USA), NASA Goddard Space Flight Center (USA), Rutherford Appleton Laboratory (UK), University of Birmingham (UK), Max-Planck-Institut für Sonnensystemforschung (Germany), Centre Spatiale de Liège (Belgium), Institut d'Optique Théorique et

Applique (France), and Institute d'Astrophysique Spatiale (France). The USA institutions were funded by NASA; the UK institutions by the Science & Technology Facility Council (which used to be the Particle Physics and Astronomy Research Council, PPARC); the German institutions by Deutsches Zentrum für Luft- und Raumfahrt e.V. (DLR); the Belgian institutions by Belgian Science Policy Office; and the French institutions by Centre National d'Etudes Spatiales (CNES) and the Centre National de la Recherche Scientifique (CNRS). The NRL effort was also supported by the USAF Space Test Program and the Office of Naval Research.

References

Amari, T., Luciani, J.F., Mikic, Z., Linker, J.A.: 2000, *Astrophys. J.* **529**, L49.
Amari, T., Luciani, J.F., Aly, J.J., Mikic, Z., Linker, J.A.: 2003a, *Astrophys. J.* **585**, 1073.
Amari, T., Luciani, J.F., Aly, J.J., Mikic, Z., Linker, J.A.: 2003b, *Astrophys. J.* **595**, 1231.
Aschwanden, M.J.: 2004, *Physics of the Solar Corona – An Introduction*, Praxis/Springer, Chichester/New York.
Aschwanden, M.J.: 2009a. In: Cheung, M., Lites, B., Magara, T., Mariska, J., Reeves, K. (eds.), *Second Hinode Science Meeting: Beyond Discovery – Toward Understanding*, Astron. Soc. Pac., San Francisco, in press.
Aschwanden, M.J.: 2009b, *Space Sci. Rev.* in press.
Aschwanden, M.J., Alexander, D.: 2001, *Solar Phys.* **204**, 91.
Aschwanden, M.J., Terradas, J.: 2008, *Astrophys. J.* **686**, L127.
Aschwanden, M.J., Fletcher, L., Schrijver, C., Alexander, D.: 1999, *Astrophys. J.* **520**, 880.
Aschwanden, M.J., Wuelser, J.P., Nitta, N., Lemen, J.: 2008a, *Astrophys. J.* **679**, 827.
Aschwanden, M.J., Nitta, N.V., Wuelser, J.P., Lemen, J.R.: 2008b, *Astrophys. J.* **680**, 1477.
Aschwanden, M.J., Wuelser, J.P., Nitta, N., Lemen, J., Sandman, A.: 2009a, *Astrophys. J.* **695**, 12.
Aschwanden, M.J., Nitta, N.V., Wuelser, J.P., Lemen, J.R., Sandman, A., Vourlidas, A., Colaninno, R.C.: 2009b, *Astrophys. J.* submitted.
Attrill, G.D.R., Harra, L.K., van Driel-Gesztelyi, L., Demoulin, P., Wuelser, J.P.: 2007, *Astron. Nachr.* **328/8**, 760.
Berger, T.E., DePontieu, B., Fletcher, L., Schrijver, C.J., Tarbell, T.D., Title, A.M.: 1999, *Solar Phys.* **190**, 409.
Bewsher, D., Harrison, R.A., Brown, D.S.: 2008, *Astron. Astrophys.* **478**, 897.
Billings, D.E.: 1966, *A Guide to the Solar Corona*, Academic Press, New York.
Chen, J.: 1997, *Astrophys. J.* **409**, L191.
Chen, P.F., Shibata, K.: 2000, *Astrophys. J.* **545**, 524.
Chen, J., Santori, R.A., Krall, J., Howard, R.A., Duffin, R., Moses, J.D., Brueckner, G.E., Darnell, J.A., Burkepile, J.T.: 2000, *Astrophys. J.* **533**, 481.
Chifor, C., Isobe, H., Mason, H.E., Hannah, I.G., Young, P.R., Del Zanna, G., Krucker, S., Ichimoto, K., Katsukawa, Y., Yokoyama, T.: 2008, *Astron. Astrophys.* **491**, 279.
DeRosa, M.L., Schrijver, C.J., Barnes, G., Leka, K.D., Lites, B.W., Aschwanden, M.J., McTiernan, J.M., Regnier, S., Thalmann, J., Valori, G. *et al.*: 2009, *Astrophys. J.* in press. arXiv:0902.1007.
Fan, Y., Gibson, S.E.: 2003, *Astrophys. J.* **589**, L105.
Fan, Y., Gibson, S.E.: 2004, *Astrophys. J.* **609**, 1123.
Feng, L., Inhester, B., Solanki, S.K., Wiegelmann, T., Podlipnik, B., Howard, R.A., Wuelser, J.P.: 2007, *Astrophys. J.* **671**, L205.
Howard, R.A., *et al.*: 2008, *Space Sci. Rev.* **136**, 67.
Gissot, S.F., Hochedez, J.F., Chainais, P., Antoine, J.P.: 2008, *Solar Phys.* doi:10.1007/s11207-008-9270-0.
Kliem, B., Titov, V.S., Török, T.: 2004, *Astron. Astrophys.* **413**, L23.
Klimchuk, J.A., Patsourakos, S., Cargill, P.J.: 2008, *Astrophys. J.* **682**, 1351.
Krall, J., Chen, J., Santoro, R.: 2000, *Astrophys. J.* **539**, 964.
Krucker, S., Lin, R.P.: 2008, *Astrophys. J.* **673**, 1181.
Illing, R.M.E., Hundhausen, A.J.: 1986, *J. Geophys. Res.* **91**, 10951.
Li, Y., Lynch, B.J., Stenborg, G., Luhmann, J.G., Huttunen, K.E.J., Welsch, B.T., Liewer, P.C., Vourlidas, A.: 2008, *Astrophys. J.* **681**, L37.
Lin, R.P., *et al.*: 2002, *Solar Phys.* **210**, 3.
Linker, J.A., Mikic, Z.: 1995, *Astrophys. J.* **438**, L45.
Long, D.M., Gallagher, P.T., McAteer, R.T.J., Bloomfield, D.S.: 2008, *Astrophys. J.* **680**, L81.
Mikic, Z., Linker, J.A.: 1994, *Astrophys. J.* **430**, 898.
Nakariakov, V.M., Ofman, L., DeLuca, E., Roberts, B., Davila, J.M.: 1999, *Science* **285**, 862.

Noglik, J.B., Walsh, R.W., Maclean, R.C.: 2008, *Astrophys. J.* submitted. arXiv:0807.4487.
Patsourakos, S., Pariat, E., Vourlidas, A., Antiochos, S.K., Wuelser, J.P.: 2008, *Astrophys. J.* **680**, L73.
Raftery, C.L., Gallagher, P.T., Milligan, R.O., Klimchuk, J.A.: 2009, *Astron. Astrophys.* **494**, 1127.
Raouafi, N.E., Petrie, G.J.D., Norton, A.A., Henney, C.J., Solanki, S.K.: 2008, *Astrophys. J.* **682**, L137.
Sandman, A., Aschwanden, M.J., Wuelser, J.P., DeRosa, J., Alexander, D.: 2009, *Solar Phys.* in press.
Schrijver, C.J., Aschwanden, M.J., Title, A.: 2002, *Solar Phys.* **206**, 69.
Schrijver, C.J., Title, A.M., Berger, T.E., Fletcher, L., Hurlburt, N.E., Nightingale, R.W., Shine, R.A., Tarbell, T.D., Wolfson, J., Golub, L., *et al.*: 1999, *Solar Phys.* **187**, 261.
Steinolfson, R.S., Hundhausen, A.J.: 1988, *J. Geophys. Res.* **93**, 14269.
Török, T., Kliem, B.: 2003, *Astron. Astrophys.* **406**, 1043.
Török, T., Kliem, B., Titov, V.S.: 2003, *Astron. Astrophys.* **413**, L27.
Veronig, A.M., Temmer, M., Vrsnak, B.: 2008, *Astrophys. J.* **681**, L113.
Verwichte, E., VanDoorsselaere, T., Aschwanden, M.J., Foullon, C., Nakariakov, V.M.: 2009, *Astrophys. J.* in press.
Vourlidas, A., Howard, R.A.: 2008, *Astrophys. J.* **642**, 1216.
Wu, S.T., Guo, W.P.: 1997, *Adv. Space Res.* **20/12**, 2313.
Wuelser, J.P., Lemen, J.R., Tarbell, T.D., Wolfson, C.J., Cannon, J.C., Carpenter, B.A., Duncan, D.W., Gradwohl, G.S., Meyer, S.B., Moore, A.S., *et al.*: 2004, *Proc. SPIE* **5171**, 111.
Yeh, T., Wu, S.T.: 1991, *Solar Phys.* **132**, 335.